

A Panoramic H α Imaging Survey of the $z=0.4$ cluster Cl 0024.0+1652 with Subaru

Tadayuki Kodama¹, Michael L. Balogh^{2,3}, Ian Smail², Richard G. Bower² & Fumiaki Nakata²

¹ National Astronomical Observatory of Japan, Mitaka, Tokyo 181-8588, Japan

² Institute for Computational Cosmology, University of Durham, South Road, Durham, DH1 3LE, UK

³ Present address: Department of Physics, University of Waterloo, Waterloo, ON, Canada N2L 3G1

12 May 2019

ABSTRACT

We employ panoramic, multicolour (BRz') and narrow-band H α imaging of the cluster Cl 0024.0+1652 ($z = 0.39$) from Subaru covering a ~ 30 arcmin field, to determine cluster membership and star formation rates for a large sample of galaxies across a wide field in the cluster, ~ 10 Mpc. We use photometric redshifts to identify cluster members, and statistically correct for the residual field contamination using similar data from the Subaru Deep Field. We detect over 500 galaxies in narrow-band emission, with broad-band colours consistent with them lying at $z \sim 0.39$. Using this sample we determine the H α luminosity function within the cluster and find that its form is approximately independent of local density, and is consistent with that seen in the intermediate redshift field population. This suggests that any density-dependent physical mechanisms which alter the star formation rate must leave the H α luminosity function unchanged; this is possible if the time-scale for star formation to cease completely is short compared with a Hubble time. Such short time-scale transformations are also supported by the presence of a population with late-type morphologies but no detectable H α emission. The fraction of blue galaxies, and the fraction of galaxies detected in H α , decreases strongly with increasing galaxy density in a manner which is qualitatively similar to that seen at lower redshifts. This trend is significantly steeper than the trend with galaxy morphology observed from a panoramic *Hubble Space Telescope* image of this cluster; this suggests that the physical mechanisms responsible for transformations in morphology and star formation rates may be partially independent. Finally, we compare our data with similar data on clusters spanning a range of redshifts from $0.2 \lesssim z \lesssim 0.8$ and find little evidence for a trend in the total amount of star formation in clusters with redshift. Although the data can accommodate strong evolution, the scatter from cluster to cluster at fixed redshift is of a comparable magnitude.

Key words: galaxies: clusters — galaxies: evolution — galaxies: clusters: individual Cl 0024.0+1652

1 INTRODUCTION

The correlation between average stellar population age, star formation rate, and galaxy environment at low redshift has recently been established quantitatively, thanks to large redshift surveys (Lewis et al. 2002; Gomez et al. 2003; Hogg et al. 2004; Baldry et al. 2004; Balogh et al. 2004b). To first order, the galaxy population is made up of two types: one with blue stellar populations and active star formation, and a second, quiescent one with redder colours. Although the average colour and star formation rate of the blue pop-

ulation is approximately independent of environment, the relative fraction of these galaxies decreases strongly as the local galaxy density increases (Balogh et al. 2004a,b). This correlation exists on all density scales, even in low-density regions well outside the cores of rich clusters.

The next step is to measure how these relationships evolve with time. Butcher & Oemler (1978a) were the first to present convincing evidence that galaxies in dense cluster cores were bluer in the recent past than they are today. However, the subsequent detection of a similar type of evolution in the general field population (Lilly et al. 1996)

means that we do not know how much of this evolution is due to external forces (i.e. the environment) and how much is due to normal galaxy evolution by, for example, the gradual consumption of available cold gas. To resolve this question requires measurements of the correlation between galaxy stellar populations and environment at a series of redshifts. Early attempts at this used sparsely sampled redshift surveys of clusters to correlate galaxy star formation rates with environment (e.g. Balogh et al. 1997; Fisher et al. 1998; Poggianti et al. 1999). These studies showed that, even at $z \sim 0.5$ there are few emission line galaxies within clusters, relative to the surrounding field, even ~ 1 Mpc from the cores. In particular, they find relatively large populations of red galaxies with mid/late-type disk morphologies but no signs of star formation; such galaxies are rarely seen in the field (Poggianti et al. 1999). Unfortunately, the limited fields of view of these studies meant it was impossible to identify where the star formation in in-falling field galaxies is terminated, or to relate this to any changes in their morphologies. A key requirement for making progress is to trace the star-forming population within clusters across very large distances and hence a wide range of environments, out to the turn-around radius (> 5 Mpc).

Most observations of clusters at intermediate redshift have relied on the $[\text{OII}]\lambda 3727$ emission line as a tracer of star formation. As has frequently been pointed out, the $[\text{OII}]$ emission is severely affected by dust extinction and metallicity; thus, another explanation of the apparently passive, red spiral galaxies in distant clusters could be that they are more highly extincted or metal-poor than disk galaxies in the field. For this reason, $\text{H}\alpha$ has been more recently used to study the distribution of star formation within high-density environments, particularly at $z < 0.5$ where the observed wavelength lies in the visible spectrum. One such programme which obtained a deeper, more complete measurement of the star formation activity in clusters involved deep, ultraplex spectroscopic surveys of narrow wavelength ranges, targeting $\text{H}\alpha$ emission in clusters at $z \sim 0.2\text{--}0.3$ (Couch et al. 2001; Balogh et al. 2002b). This provides a very sensitive probe of the $\text{H}\alpha$ luminosity function on ~ 7 arcmin (2–4 Mpc) scales within intermediate redshift clusters. These measurements have shown that, while the fraction of galaxies detected in $\text{H}\alpha$ remains low even ~ 1 Mpc from the cluster centre, at least the shape of the bright end of the $\text{H}\alpha$ luminosity function is approximately independent of environment.

One particularly powerful approach to surveying $\text{H}\alpha$ within clusters is to use narrow-band imaging to trace $\text{H}\alpha$ emitting galaxies over very wide fields in a narrow redshift slice (e.g. Fujita et al. 2003; Umeda et al. 2004; Finn et al. 2004). Narrow-band imaging has the advantages that it traces the two-dimensional distribution of instantaneous star formation, yields the total star formation rate (SFR) independent of aperture effects, and is complete (flux-limited) over very large fields and hence a wide range of environments. However, these studies do not have the high-resolution imaging over a comparable field, necessary to identify the galaxies with late-type morphologies but low star formation rates that might be indicative of a transformation in progress.

In this paper, we present multicolour (broad-band and narrow-band $\text{H}\alpha$) Suprime-Cam observations over a ~ 9.6

Mpc field around the cluster Cl0024.0+1652 (Cl0024) at $z = 0.395$. We use the broad-band colours to identify cluster members, and to trace the young stellar population, while the narrow-band $\text{H}\alpha$ imaging follows the instantaneous star formation rate. Importantly, a large *Hubble Space Telescope* (*HST*) mosaic, consisting of 39 WFPC2 pointings, is available. Analysis of these data has shown that the fraction of early type galaxies increases steeply from ~ 1 Mpc toward the cluster centre (Treu et al. 2003). The combination of these high resolution images with our new $\text{H}\alpha$ data provides a unique opportunity to study the effects of environment on morphology and star formation rate, separately.

Cl0024 is one of the original clusters studied by Butcher & Oemler (1978a,b), and later followed up spectroscopically (Couch & Newell 1984; Dressler & Gunn 1982, 1992; Dressler et al. 1999; Poggianti et al. 1999; Czoske et al. 2001). From the lensing analysis of Kneib et al. (2003), the characteristic radius of the cluster is $R_{200} = 1.7$ Mpc, and the total mass within this radius is $5.7 \times 10^{14} M_{\odot}$. The cluster core is dominated by red galaxies, with a secondary population of spiral galaxies that are mostly unremarkable (Schneider, Dressler, & Gunn 1986), though some show evidence for recent starbursts (Koo et al. 1997; Poggianti et al. 1999), perhaps enshrouded in dust (Coia et al. 2004). The red galaxies follow the fundamental plane relation (van Dokkum & Franx 1996), and are consistent with passive evolution models (Kodama et al. 1998; Barger et al. 1998). Earlier *HST* imaging (Smail et al. 1997) revealed a clear lack of S0 galaxies relative to nearby clusters (Dressler et al. 1997), which has been used as an argument that the S0 population is being formed within such clusters, between $z \sim 0.4$ and the present. Recent, wide-field spectroscopy of a very large sample of cluster galaxies by Czoske et al. (2001) has identified substructures in the foreground and background of Cl0024. They find the velocity dispersion of the main cluster component is only $\sim 560 \text{ km s}^{-1}$, much less than earlier measurements of $\sim 1200 \text{ km s}^{-1}$ (Dressler & Gunn 1992) which did not resolve the substructure. This spectroscopic sample of cluster galaxies is the largest available for any cluster at $z \gtrsim 0.2$ and enables us to perform a number of powerful tests of the reliability of our narrow-band selected sample.

The present paper is organized as follows. Our observations and data reduction are presented in § 2, and the measurements of $\text{H}\alpha$ emission and derived quantities are described in § 3. The spatial distribution and environmental variation in galaxy populations are shown in § 4. We discuss the implications of these results for galaxy evolution in general, in § 5, and draw our final conclusions in § 6. Throughout this work we assume a cosmology with $\Omega_m = 0.3$, $\Omega_{\Lambda} = 0.7$, $H_0 = 70 \text{ km s}^{-1} \text{ Mpc}^{-1}$. At the redshift of Cl0024, $z = 0.395$, 1 arcmin corresponds to 0.32 Mpc, and the characteristic luminosity M^* is $z' \sim 19.2$.

2 OBSERVATIONS AND DATA REDUCTION

Data were obtained with Suprime-Cam (0.202 arcsec per pixel, and 27 arcmin field of view) on the Subaru telescope on the night of September 6, 2002. Images were obtained in three broad-band filters (BRz'), and the narrow band filter NB_{912} ($\lambda_{\text{eff}} = 9139 \text{ \AA}$, $\text{FWHM} = 134 \text{ \AA}$). The net expo-

sure times are 60 min in B , 88 min in R , 33 min in z' and 180 min in NB $_{912}$. We took two exposures in z' , a deep one (4 min) and a shallow one (1 min); the latter was required because the brightest galaxies ($z' < 21$) are saturated on the deep image. The 5- σ limiting magnitude of the z' images, on which our selection is based, is 22.7 mag, corresponding to $M^* + 3.5$ at the cluster redshift. The seeing was 0.7–1.0 arcsec in the R , z' and NB $_{912}$ bands, but worse (~ 1.0 –1.3 arcsec) in the B -band. The sky conditions were photometric, and the photometric zero-points were calibrated based on the Landolt (1992) standard stars in B and R ; the z' -band image was calibrated onto the SDSS system using the star G24-9. The data were reduced with the IRAF and NEKOSOFT (Yagi 1998) software packages, following standard procedures of bias subtraction and flat-fielding. The latter is achieved using supersky flats constructed from the median of the dithered science frames. We then mosaic the chips, taking care to match the point-spread function (PSF) and relative flux calibration between them.

The relative transmission function of the narrow band filter NB $_{912}$ combined with the response of the CCD is shown in Fig. 1. The effective wavelength and width are 9139 Å and 134 Å, respectively. This response function is compared with the velocity distribution of spectroscopically confirmed cluster members in our target, Cl 0024, from Czoske et al. (2001). At the peak of the observed galaxy redshift distribution, the H α emission line lies at $\lambda \sim 9160$ Å, close to the maximum filter transmission. The galaxy redshift distribution is significantly narrower than NB $_{912}$, so we have good sensitivity for all cluster members. Note that the foreground and background structures detected by Czoske et al. (2001) lie in regions of lower filter transmission, so our H α detection limit will be brighter in these structures.

Galaxies are detected from the z' images, using the SExtractor software (Bertin & Arnouts 1996). We detect all objects with at least 9 connected pixels (0.38 arcsec 2 , equivalent to the area of the PSF) more than 2 σ above the median sky. The images in all filters are aligned by centroiding stars throughout the field and fitting a stretch and shift. The images are each convolved with a Gaussian to mimic a seeing of 1.0 arcsec, corresponding to that of our poorest quality data in the R and z' -bands. The seeing on the B -band images is slightly worse, and these are convolved to 1.3 arcsec. As a result, the FWHM of the stars are not uniform between the passbands; however, as we use a fixed 3 arcsec aperture (corresponding to 16 kpc at the cluster redshift) when measuring galaxy colours, this small mismatch in the seeing sizes produces a negligible difference in the measured colours. The magnitude MAG_BEST is used as a measure of total magnitude. All the magnitudes in this paper are given in the Vega-based system.

We will use the Subaru Deep Field (SDF, Maihara et al. 2001) as a control field, to correct for residual background contamination after photometric membership selection (e.g. Kodama et al. 2001). This imaging was reduced using similar techniques, and has an effective area of 667.94 sq. arcmin. These observations include the same broad band filters that we use, and also a similar narrow-band filter, with a central wavelength of 9196 Å and an effective FWHM of 132 Å.

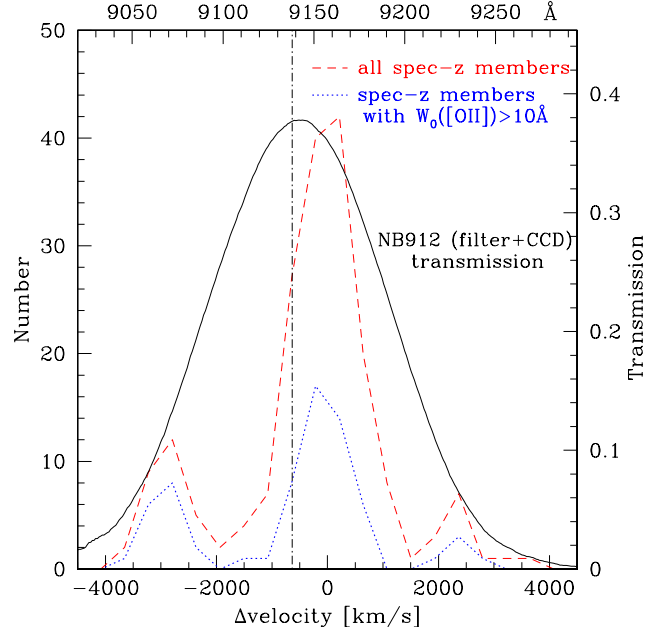


Figure 1. The dashed line is the velocity distribution of spectroscopically confirmed cluster members in Cl 0024, from Czoske et al. (2001); the dotted curve is the distribution for those members with [OII]λ3727 emission. The top axis shows the corresponding wavelength of H α . The throughput of the narrow-band filter NB $_{912}$, including the response of the CCD, as a function of velocity is shown as the solid curve, according to the scale on the right axis.

3 H α MEASUREMENTS AND FIELD SUBTRACTION

3.1 Continuum subtraction and detection criteria

Emission line fluxes are measured by comparing the aperture magnitudes in the NB $_{912}$ and z' bands, as shown in Fig. 2. We determine the zero-point of the NB $_{912}$ filter by requiring the mean ($z' - \text{NB}_{912}$) colour to be zero for stars and spectroscopic non-members. Fig. 2 shows that most detected galaxies have $(z' - \text{NB}_{912}) \sim 0$, with a scatter that increases toward fainter magnitudes. This is expected, because most galaxies are in the foreground or background, and H α does not lie within our filter bandpass; the scatter is primarily due to photometric errors. Since the equivalent widths of stellar H α absorption lines in non-star forming galaxies are typically only ~ 2 Å (e.g. Trager et al. 1998), we can assume the envelope of galaxies at $(z' - \text{NB}_{912}) < 0$ traces the intrinsic scatter due to measurement uncertainty; this envelope is approximated by the dotted lines in Fig. 2, given by $(z' - \text{NB}_{912}) > 0.044(z' - 21.6) + 0.2$ for $z' < 21.6$, and $(z' - \text{NB}_{912}) > 0.273(z' - 21.6) + 0.2$ for $z' \geq 21.6$. There are 753 galaxies lying above this line that represent significant detections; however, some of these will correspond to emission from background galaxies, in lines other than H α . We make a correction for these based on broad-band colours, as described in § 3.3.

Since the NB $_{912}$ filter has a Gaussian profile and is slightly offset from the wavelength of H α at the cluster redshift, we must account for the lower transmission of the NB $_{912}$ filter for a typical cluster galaxy. We correct for this,

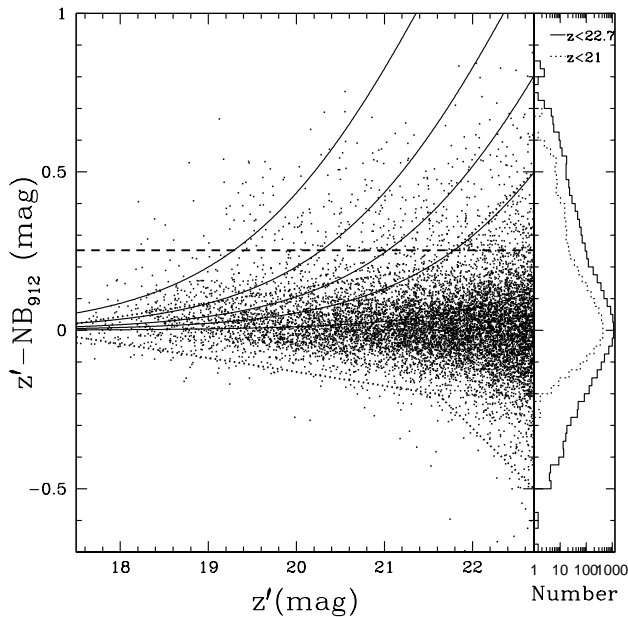


Figure 2. The distribution of galaxies in $\text{NB}_{912}-z'$ colour, as a function of z' magnitude for all galaxies in the photometric catalogue. The curved, solid lines show lines of constant $\text{H}\alpha$ luminosity from $L(\text{H}\alpha+\text{[NII]}) = 0.66, 3.3, 6.6, 13.2$ and 33×10^{40} ergs s^{-1} , increasing towards higher $z'-\text{NB}_{912}$. These correspond to SFR, in units of $M_{\odot} \text{ yr}^{-1}$, of 0.1, 0.5, 1.0, 2.0 and 5.0, respectively. The diagonal, dotted lines show the envelope of the observed scatter; the 753 galaxies that lie above the upper line are secure emission line detections, although we estimate that ~ 240 are likely to be background galaxies on the basis of BRz' colour-colour diagram (see § 3.2 and Fig. 7). For galaxies with $z' < 21.8$, the sample of detections is complete to $W_o(\text{H}\alpha+\text{[NII]}) = 40 \text{ \AA}$, shown as the horizontal, dashed line. The histograms on the right show the distribution of $(z' - \text{NB}_{912})$ for all galaxies in the sample, brighter than $z' = 22.7$ (solid line) and $z' = 21$ (dotted line).

in an average sense, by multiplying our measured $\text{H}\alpha$ fluxes and equivalent widths (see § 3.2) by a factor 1.37, compensating for the throughput averaged over the spectroscopic cluster members in the Czoske sample, as shown in Fig. 1. On an individual galaxy basis, however, the $\text{H}\alpha$ flux for cluster members is uncertain by ~ 15 per cent, due to the variable filter throughput over 1000 km s^{-1} . We have also checked our results for sensitivity to colour terms; however we neglect this correction as it is small relative to our photometric uncertainties.

3.2 Computation of $W_o(\text{H}\alpha+\text{[NII]})$ and $\text{H}\alpha$ fluxes

The emission lines $\text{[NII]}\lambda\lambda 6548, 6583$ are adjacent to $\text{H}\alpha$, and also contribute to the emission line flux within NB_{912} . Instead of making an uncertain correction for this based on empirical calibrations (e.g. Tresse et al. 1999), we choose to present most of our results for the combined line flux, and only make a correction when computing SFRs. To compute the rest frame equivalent width, $W_o(\text{H}\alpha+\text{[NII]})$, from $(z' - \text{NB}_{912})$, we need to correct for the effect of emission within the broad-band filter. The conversion depends on the relative wavelength ranges of the z' filter ($\Delta\lambda_{BB} = 1360 \text{ \AA}$)

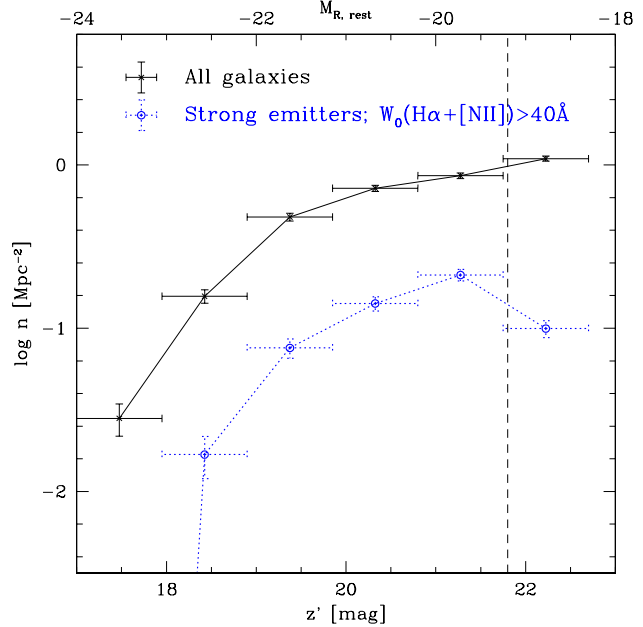


Figure 3. The differential number count of galaxies in the z' -band. The solid line and the dotted line show all the galaxies and those with strong emissions, respectively. The vertical dashed line represents $z' = 21.8$ below which our detection of strong emitters become incomplete due to large photometric errors.

and narrow-band filter ($\Delta\lambda_{NB} = 134 \text{ \AA}$), and is given by:

$$W_o(\text{H}\alpha + \text{[NII]}) = (1+z)^{-1} \times \frac{\Delta\lambda_{BB}\Delta\lambda_{NB}(r-1)}{\Delta\lambda_{BB} - \Delta\lambda_{NB}r}, \quad (1)$$

where $\log_{10}(r) = (z' - \text{NB}_{912})/2.5$ and $z = 0.395$ is the cluster redshift. To calculate $\text{H}\alpha+\text{[NII]}$ fluxes we multiply $W_o(\text{H}\alpha+\text{[NII]})$ by the continuum z' luminosity (on the Vega system, $z' = 19.2$ corresponds to a flux of 1.636×10^{-17} ergs $\text{s}^{-1}\text{cm}^{-3}\text{\AA}^{-1}$). In Fig. 2 we show the horizontal line corresponding to $W_o(\text{H}\alpha+\text{[NII]}) = 40 \text{ \AA}$; at all magnitudes brighter than $z' = 21.8$, galaxies with equivalent widths greater than this limit are significantly detected in emission (see also Fig. 3). We will therefore use this magnitude limit when considering the fraction of galaxies with $W_o(\text{H}\alpha+\text{[NII]}) > 40 \text{ \AA}$, as in § 4.4.

We then compute total luminosities, $L(\text{H}\alpha+\text{[NII]})$, using a luminosity distance of 2147 Mpc, appropriate for our cosmological model. Finally, we compute SFRs assuming the conversion of Kennicutt et al. (1994), correcting for 30% [NII] emission (Tresse et al. 1999; Jansen et al. 2000) and an extinction at $\text{H}\alpha$ of 1 magnitude (Kennicutt et al. 1994). Both of these corrections are uncertain, and only accurate in an average sense, for reasonably bright galaxy populations ($\gtrsim M^* + 1$) with metallicities above ~ 0.5 solar (Brinchmann et al. 2003; Kewley, Geller, & Jansen 2004).

In Fig. 4 we show the correlation between our measured equivalent widths, $W_o(\text{H}\alpha+\text{[NII]})$, and the $[\text{OII}]$ equivalent widths from Czoske et al. (2001), for spectroscopically confirmed cluster members. The correlation is in reasonable agreement with the local relation from Kennicutt (1992), with considerable scatter. Some of this scatter is due to the ~ 15 per cent uncertainty on the NB_{912} filter throughput. The $W_o(\text{H}\alpha)$ for galaxies with redshifts $> 2000 \text{ km s}^{-1}$ from

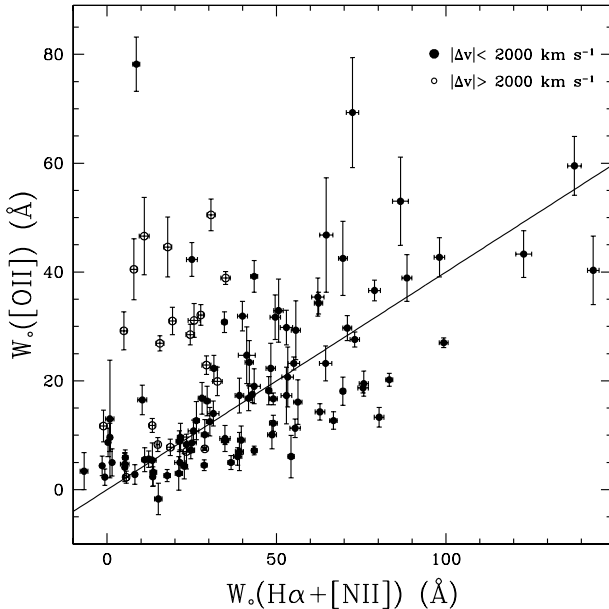


Figure 4. The correlation between our measured $W_o(H\alpha+[NII])$ and the spectroscopically measured $W_o([OII])$ from Czoske et al. (2001). Solid circles are galaxies with redshifts within 2000 km s^{-1} of the peak of filter transmission function, while open circles are galaxies with velocity differences greater than this. The solid line is the local relation, from Kennicutt (1992).

the peak of the NB₉₁₂ filter ($\lambda = 9140 \text{ \AA}$, corresponding to $z = 0.393$ for H α) are underestimated by typically a factor of $2 \times$, due to the lower filter transmission. These galaxies are shown as the open circles in Fig. 4, and all have low $W_o(H\alpha)$ for their measured $W_o([OII])$. From Fig. 1 it is evident that these galaxies correspond to the dynamically distinct foreground and background clumps, and not the main body of the cluster.

Recently, Coia et al. (2004) presented *Infrared Space Observatory (ISO)/CAM* mid-infrared observations of the central ~ 2 arcmin of Cl0024 at $15\mu\text{m}$. They identify thirteen mid-infrared sources which are confirmed cluster members (within the main cluster, not the foreground and background substructures), and they are able to derive star formation rates for twelve of them. Two of these detections are not in our catalogue because of corrupted photometry in our image, while a third is excluded because z_{phot} is outside our membership limits, and z_{spec} is flagged as uncertain (see § 3.3). Of the remaining 9 galaxies, 6 are detected in H α ; we compare the SFR estimated from H α (assuming 1 mag extinction) with that estimated from the mid-infrared, in Fig. 5. For all of the *ISO* sources that we detect in emission, the H α -derived SFRs are within a factor of $\sim 2\text{--}3$ of the mid-infrared estimates. For the three remaining galaxies, the infrared SFRs are larger than those determined from H α , by at least a factor $\sim 3\text{--}10$. This discrepancy is likely due to a wide range of extinctions among strongly star-forming galaxies (Hopkins et al. 2001, 2003; Afonso et al. 2003), and implies that the extinction for these galaxies is $\gtrsim 2.5$ mag at H α . Another possibility is that at least some of the mid-infrared emission in these sources arises from a nonthermal component (e.g. Balogh et al. 2002b).

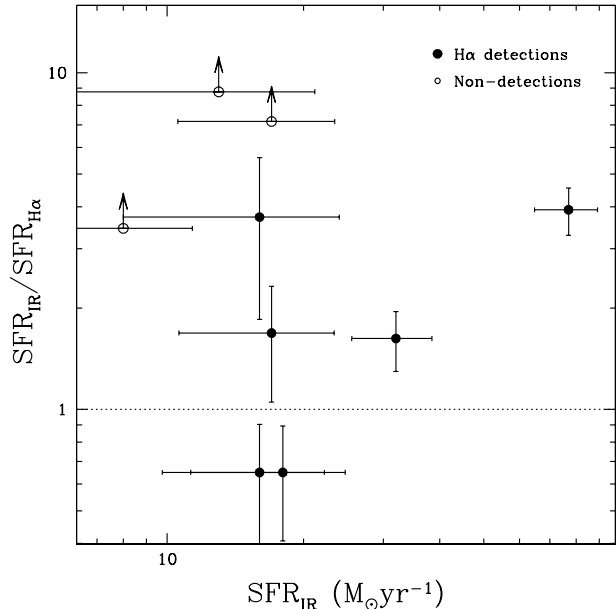


Figure 5. The ratio of the SFR estimated from mid-infrared *ISO/CAM* observations (Coia et al. 2004) to that measured from our H α photometry. The solid circles are H α detections, and the open circles are non-detections. Four ISO-detected galaxies are not included in this comparison for reasons discussed in the text, and thus do not appear on the plot.

3.3 Photometric redshifts and field contamination

To determine cluster membership for all of the galaxies within our imaging field of view we use broad-band colours to compute photometric redshifts, z_{phot} , using the code of Kodama, Bell, & Bower (1999). The reliability of these redshifts can be tested by comparing with the spectroscopic catalogue of Czoske et al. (2001). Fig. 6 shows the distribution of z_{phot} for spectroscopically confirmed cluster members ($0.378 < z < 0.406$). We note that this redshift range for spectroscopic members is set so that the transmission of our narrow-band filter is better than 8% for the H α lines from those galaxies. This corresponds to the velocity range of $-3400 < \Delta v < 2300 \text{ km s}^{-1}$ and therefore it includes a significant fraction of the substructures reported in Czoske et al. (2001) (see our Fig. 1). As seen in Fig. 6, most of the members have $0.31 < z_{\text{phot}} < 0.45$; however, there is a small tail of galaxies for which the photometric redshift is $z < 0.3$. These are preferentially blue galaxies, for which photometric redshifts are less accurate due to their flat spectra.

We want to ensure our sample of H α detections is not compromised by incorrect photometric redshifts for blue galaxies. We can do this by noting that a detected emission line is most likely to be either H α at $z \sim 0.4$, [OIII] $\lambda 5007$ at $z \sim 0.8$ or [OII] $\lambda 3727$ at $z \sim 1.5$. Distinguishing these redshifts photometrically is relatively easy, as shown in Fig. 7. The position of galaxies in the $(R - z') - (B - R)$ colour plane, as a function of redshift, spectral type, and metallicity, are computed using the models of Kodama, Bell, & Bower (1999). We also show the data, for all galaxies detected in NB₉₁₂; these show a dominant sequence close to the model prediction for H α emission, with distinct, secondary

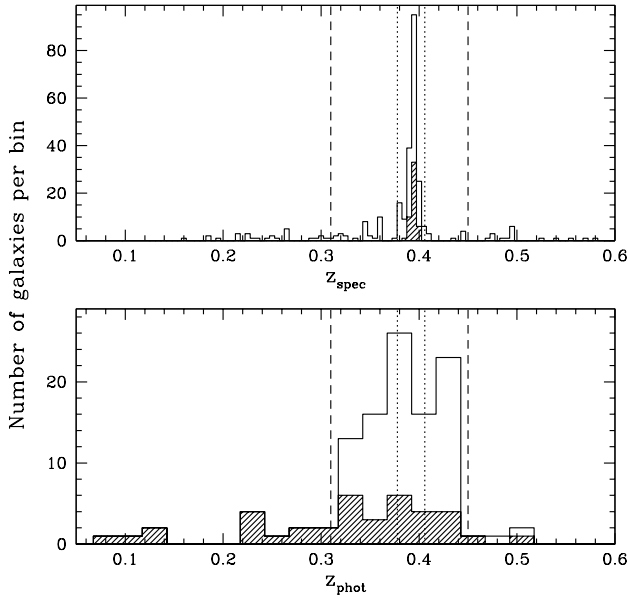


Figure 6. Bottom panel: The photometric redshift distribution for the spectroscopically confirmed members is shown as the open histogram. The spectroscopic cluster redshift limits ($0.378 < z < 0.406$) are shown as the vertical, dotted lines. The photometric redshift distribution is broader; we take the photometric redshift cluster limits to be $0.31 < z_{\text{phot}} < 0.45$, as indicated by the vertical, dashed lines. The solid histogram shows the distribution for $\text{H}\alpha$ emitters. **Top panel:** The distribution of spectroscopic redshifts for galaxies with $0.31 < z_{\text{phot}} < 0.45$, indicated by the dashed lines, is shown as the open histogram. The solid histogram shows the distribution for all $\text{H}\alpha$ emitters.

sequences corresponding to the background galaxies with [OII] or [OIII] emission. We therefore consider all 511 galaxies that are detected in the continuum-subtracted NB₉₁₂ filter and have colours within the box shown in Fig. 7 to be cluster members, whatever their photometric redshifts. We note that the higher redshift emission galaxies are distributed uniformly over the field of view compared to the emission line members, confirming that they are unlikely to be misidentified cluster members. We can use these background galaxies to construct the [OII] luminosity function at $z \sim 1.5$, which we leave for future work.

We will therefore define cluster members to be galaxies with $0.31 < z_{\text{phot}} < 0.45$, or those detected in $\text{H}\alpha$. We also include all spectroscopic members, with redshift quality flags A(secure) or B(probable), from the catalogue of Czoske et al. (2001). This combined technique of using both broad-band and narrow-band photometric selection appears to work well in picking out cluster members, as demonstrated by Fig. 6. We have a slight bias against blue member galaxies in our photometric redshifts derived purely from the broad-band data; however this is compensated by the fact that these galaxies tend to be strong emission line sources, and so are recovered by including the narrow-band filter. This combination is potentially a very powerful tool for future applications to study the whole range of spectral types in higher redshift structures using optical/near-infrared filters.

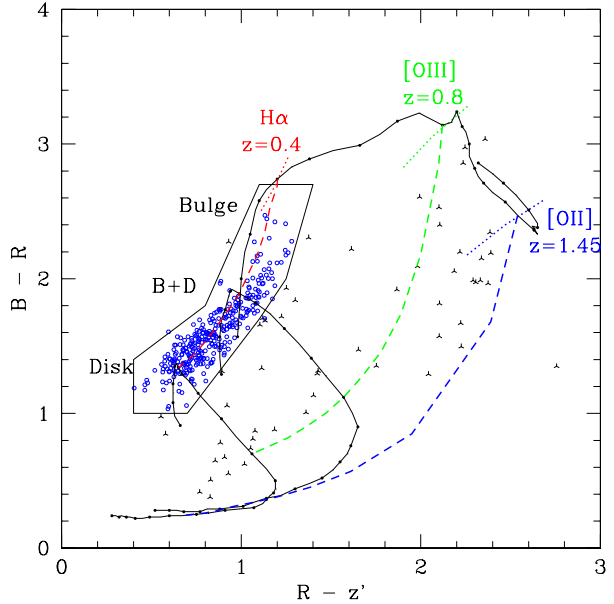


Figure 7. The colour-colour diagrams on which we can distinguish $\text{H}\alpha$ emission of the cluster members from background [OII] and [OIII] contaminants. Models of Kodama, Bell, & Bower (1999), as a function of redshift, spectral type and metallicity, are shown by the lines. Each contiguous solid line shows a model for a given spectral type, at a series of redshifts between $0 \leq z \leq 2$. The dashed lines connect the three spectral models at fixed redshifts corresponding to $\text{H}\alpha$, [OII] and [OIII] emission, as indicated. The dotted lines show the effect of changing metallicity in the pure, passive (“Bulge”) model between $-0.52 \leq [\text{M}/\text{H}] \leq 0.06$. The observed colour distribution of the strong emitters ($z' - NB_{912} > 0.25$) brighter than $z' = 21.8$ (fainter than this limit the photometric errors increasingly dilute the visible structure) in the C10024 field are plotted over the model grids. We identify the likely $\text{H}\alpha$ emitters (*open circles*) as either those whose photometric redshifts are within our membership slice or those whose colours are within the box drawn along the $z \sim 0.4$ sequence. The latter galaxies are regarded as cluster members even if they have apparently inconsistent photometric redshifts. We also show the distribution of narrow-band emitters which are not identified as cluster members (*three-point crosses*) and are thus likely to be higher redshift galaxies.

We identify 2385 cluster members defined in this way down to $z' = 22.7$, over 712.79 arcmin^2 , for a mean projected density of 33 Mpc^{-2} . Fig. 6 shows the distribution of spectroscopic redshifts for these photometric cluster members. Most of the galaxies are true cluster members ($0.378 < z < 0.406$), although ~ 30 per cent are background and foreground galaxies that are misidentified as cluster members. We correct for this residual contamination based on the control field, the Subaru Deep Field (Maihara et al. 2001). The same photometric redshift estimator is applied to galaxies in this field, observed in the same combination of passbands to estimate the number of field galaxies within the cluster redshift limits $0.31 < z_{\text{phot}} < 0.45$. We detect 1300 galaxies with magnitude $z' < 22.7$ in this redshift range, over 667.94 arcmin^2 . This corresponds to a background object density of 19 Mpc^{-2} , which is our contamination; this is statistically subtracted from our photometrically-determined

Fig. 8 is provided in jpg format.

Figure 8. The projected distribution of the photometrically-determined cluster members in Cl0024. North is top and east is to the left. Filled circles are strong emitters ($W_o(H\alpha) > 40 \text{ \AA}$) brighter than $z' = 21.8$ and the *small dots* are the others. The red and blue points separate the galaxy colours redder or bluer than $(B - R)_c = 2.0$. The contours trace lines of constant projected galaxy density, corresponding to 30, 50, 70, 100, 200 and 300 Mpc^{-2} after residual field contamination is subtracted. The virial radius of this cluster (1.7 Mpc) is shown by the dotted circle.

cluster members, as a function of magnitude and colour, as described in Kodama et al. (2001).

3.4 Local density measurements

The local surface number density of cluster members is calculated from the 10 nearest neighbors (including that galaxy) brighter than our magnitude cut, $z' = 22.7$. We correct for residual field contamination in the redshift slice by subtracting the mean density of galaxies in the control field, 19 Mpc^{-3} . Unlike complete redshift surveys, we are not sensitive to densities near or below the average field density, because the photometric redshift slice is too wide to allow us to probe low physical densities.

It will be interesting to compare our results with similar measurements in the local Universe (e.g. Lewis et al. 2002; Gomez et al. 2003; Balogh et al. 2004b). To compare projected surface densities with these surveys, we need to account for two fundamental differences in the way they are measured. The first is that, despite the background subtraction, the measured density is still a projected quantity over a large redshift slice, which corresponds to 855 Mpc (comoving). Local densities measured from redshift surveys, however, typically project over only $\pm 1000 \text{ km s}^{-1}$, which corresponds to $\sim 30 \text{ Mpc}$. The projected volume in the present survey, therefore, is ~ 30 times larger than the corresponding volume in the low redshift surveys, and we can expect our densities to be larger by a similar factor. Note however that the actual factor is likely to be smaller than this, since the galaxies would not be uniformly distributed within our redshift slice; rather they are likely to be structured in discrete redshift slices. Secondly, the present survey extends to $M^* + 3.5$, which is 2.5 mag fainter (relative to M^*) than the local Universe study of Balogh et al. (2004b). Assuming a luminosity function with faint end slope ≥ -1.05 (Blanton et al. 2003), we expect $\gtrsim 1.7$ times more galaxies in our deeper survey. Accounting for both these effects, we expect our local projected densities to be $\gtrsim 50$ times larger than those of Balogh et al. (2004b).

4 RESULTS

4.1 Spatial Distribution

The projected galaxy distribution of Cl0024 is shown in Fig. 8 for all cluster members. Contours of constant projected galaxy density are overlaid. The main cluster body, dominated by red galaxies, appears elongated in the NW–SE direction. On a larger scale, we see filamentary substructures towards the North–NW and to the East, suggesting that the cluster is still dynamically evolving by accreting galaxies/groups from its immediate surroundings. This is qualitatively similar to the distribution of galaxies around A 851 at $z = 0.41$ (Kodama et al. 2001). It is notable that the group to the NW of the cluster core shows a large fraction of galaxies detected in H α .

In Fig. 9 we show images of the strongest H α emitters within R_{200} (1.7 Mpc) and within the “infall region” $1 < R/R_{200} < 2$. In most cases we detect extended emission, suggesting that it does not exclusively arise from AGN activity. Furthermore, the H α emission generally traces the optical structure of the galaxy, although there are some galaxies in which the H α emission appears to be offset by a small amount ($\lesssim 2 \text{ kpc}$) from the continuum light.

4.2 Hubble Space Telescope Morphologies

The available wide-field *HST* mosaic imaging (Treu et al. 2003) affords us the opportunity to compare the star formation activity in Cl0024 with galaxy morphology. Since environmental effects are likely to influence morphology and star formation on different time-scales, we might expect a change in the correlation between the two properties, as a function of density and/or redshift. Unfortunately, we do not have equivalent morphological information for our control field sample, so we cannot make the field correction necessary to reliably determine the morphology distribution as a function of cluster environment for the whole sample. For galaxies that are undetected in H α , we are therefore restricted to the spectroscopically-confirmed cluster members (Czoske et al. 2001). The population of galaxies that are detected in H α , however, does not require such a correction, since we are able to identify almost all background galaxies

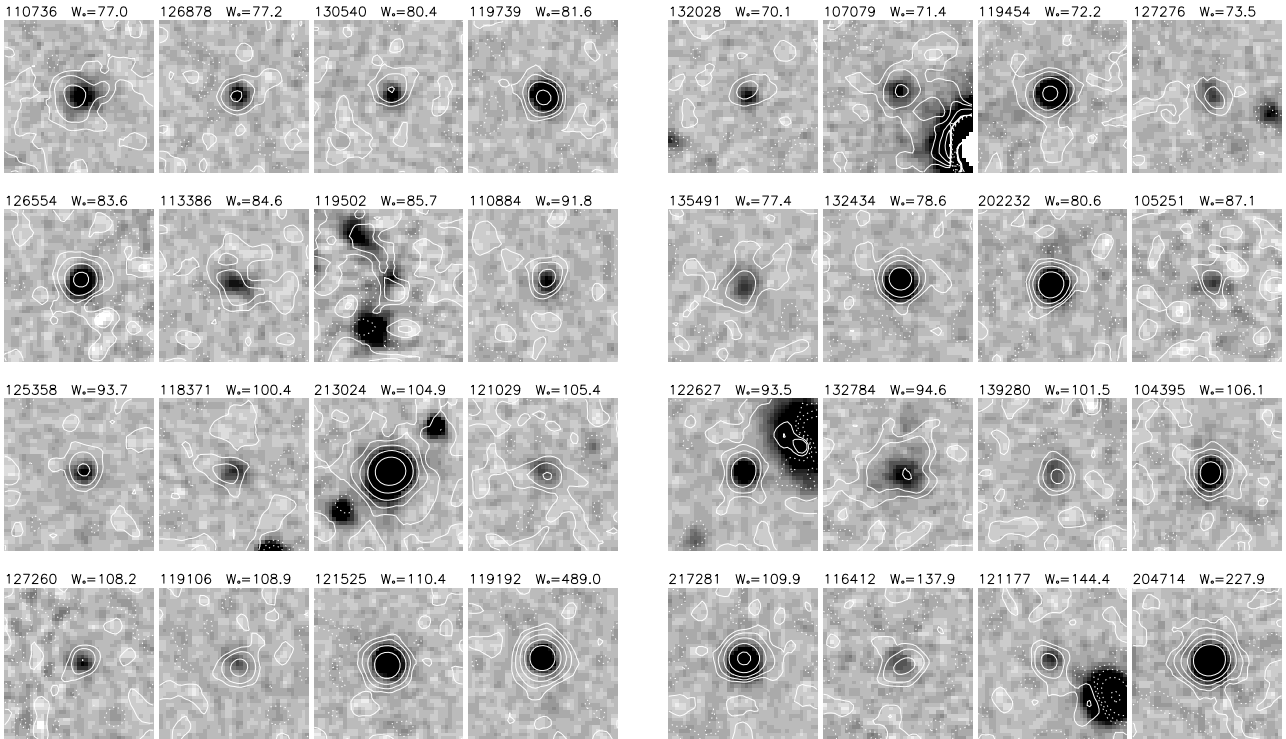


Figure 9. *Left:* The greyscale images are z' -band continuum images of galaxies within 1.7 Mpc (R_{200}) of the cluster centre with the strongest $H\alpha$ emission. Images are 8 arcsec \times 8 arcsec (42.7×42.7 kpc). North is top and east is to the left. The *solid contours* are logarithmically spaced $H\alpha$ isophotes; the *dotted contours* represent $H\alpha$ in absorption. The ID number and $W_o(H\alpha+[NII])$ of the galaxy are labelled at the top of each panel. *Right:* The same, but for galaxies within $1 < R/R_{200} < 2$.

detected in emission (see Fig. 6), and we can therefore use the full sample.

Fig. 10 shows the distribution of morphological classes for the $H\alpha$ detections and non-detections (using the scheme of Treu et al. 2003). There is a distinct separation, as expected, in that galaxies detected in $H\alpha$ tend to be late-type, while undetected galaxies are early-type. We do however see a substantial number of late-type, confirmed cluster members without $H\alpha$ emission. To investigate the morphological properties of these galaxies in more detail we show thumbnail images of 12 of the $H\alpha$ -undetected members from the late morphological classes (≥ 2) in Fig. 11 and contrast these with a random sample of $H\alpha$ -detected galaxies with the same distribution of types. The first point to note is that the two $H\alpha$ -undetected galaxies identified as mergers ($T=8$) both appear to contain early-type galaxies with very close companions. The absence of detectable $H\alpha$ emission from these systems is not particularly surprising and so we ignore them. The morphological classifications for the bulk of the mid/late-type $H\alpha$ -undetected galaxies show no strong differences from the matched sample of $H\alpha$ -detected galaxies. There is a suggestion that the $H\alpha$ -undetected galaxies may be larger systems (with 40 per cent of the sample having sizes in excess of 50 kpc). However, similarly large spirals are seen in the $H\alpha$ -detected sample and the small size of the undetected sample means this is not a statistically compelling result. Another potential difference is that none of the spiral galaxies undetected in $H\alpha$ show much evidence for bright knots or other clumpy structure associated with star-forming regions; the disks and spiral arms appear smooth.

On the other hand, such features are visible in some of the control galaxies. We discuss the $H\alpha$ -undetected population further in § 5.2.

4.3 The $H\alpha$ Luminosity function

Our sample of galaxies with $H\alpha$ emission is limited by apparent continuum magnitude and equivalent width, as shown in Fig. 2. From that figure, it is evident that our sample is approximately complete for $L(H\alpha+[NII]) > 1.3 \times 10^{41}$ ergs s^{-1} , which corresponds to $SFR \gtrsim 2 M_\odot \text{ yr}^{-1}$. Brighter than this limit, we effectively have a volume-limited sample of $H\alpha$ -selected sample of galaxies, and it is straightforward to construct the luminosity function for Cl0024. Furthermore, most of the galaxies with luminosities brighter than this limit have $z' < 21$, 1.7 magnitudes brighter than our survey limit, so the effect of photometric errors are small. At fainter line luminosities, we begin to lose bright galaxies with low $W_o(H\alpha+[NII])$ from the sample; however, the luminosity function is dominated by fainter galaxies with higher EW and, hence, the effect is small. Below $L(H\alpha+[NII]) \sim 6 \times 10^{40}$ ergs s^{-1} , our incompleteness increases further because we do not observe galaxies with $z' > 22.7$. This incompleteness starts to become severe below $L(H\alpha+[NII]) \sim 2 \times 10^{40}$ ergs s^{-1} . Photometric errors also start to become important at this luminosity, because most of the contribution is from galaxies near our magnitude limit. We make no correction for these effects, but focus on the shape of the luminosity function brighter than $L(H\alpha+[NII]) \sim 10^{41}$ ergs s^{-1} .

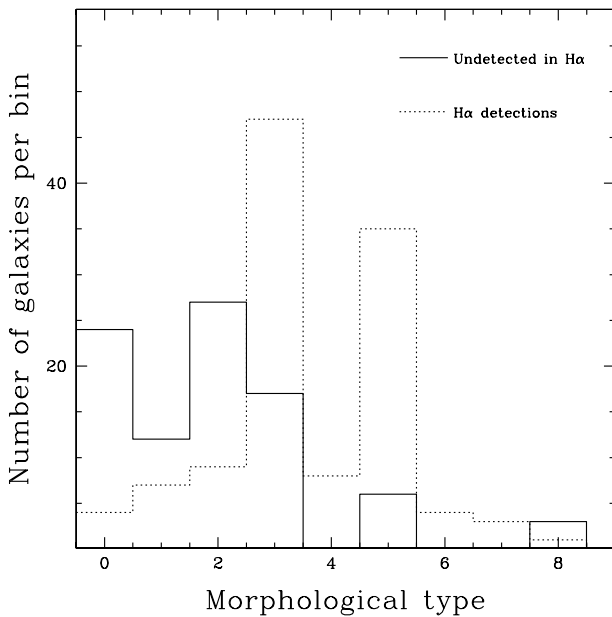


Figure 10. The distribution of morphological classes, for spectroscopic members with no detected H α emission (solid line), and all galaxies with detected H α (dotted line). The morphological classes correspond to visual morphologies as follows: 0=E, 1=E/S0, 2=S0, 3=Sa+b, 4=S, 5=Sc+d, 6=Irr, 7=unclassified, and 8=merger, respectively (Treu et al. 2003).

Fig. 11 is provided in jpg format.

Figure 11. The top three rows of the figure show thumbnail *HST* F814W images of morphologically-classified mid/late-type and merging galaxies which are spectroscopically-confirmed as cluster members, but which are not detected in our H α narrow-band survey. In the lower three rows we compare these to a randomly-selected sample of H α narrow-band detected cluster members with an identical distribution of morphological types. The two mergers appear to be early-types with close companions (their lack of H α emission is therefore unsurprising). Otherwise, the bulk of the undetected, mid-type members are morphologically indistinguishable from the detected population, with the one caveat that they appear to have larger physical scales (although the small sample means this statement is not statistically significant). Each panel is 10 arcsec square (53 kpc) and is labelled with the morphological class of the galaxy from Treu et al. (2003) and either the redshift or NB (for those members detected in the H α narrow-band image). The panels are arbitrarily orientated and are presented at the raw WFPC2 resolution, 0.17 arcsec, and default pixel scale, 0.1 arcsec pixel $^{-1}$.

The luminosity function of galaxies within $R_{200} = 1.7$ Mpc (5.2 arcmin) of the cluster centre is shown in the left panel of Fig. 12. It is well fit, for $L(H\alpha+[NII]) > 10^{41}$ ergs s $^{-1}$, by a Schechter function with $L^*(H\alpha+[NII]) = 1.1 \times 10^{42}$ ergs s $^{-1}$ and $\alpha = -1.5$. Recall that this is uncorrected for dust extinction and [NII] emission. Making an approximate correction for 1 magnitude of dust extinction and 30 per cent [NII] contribution gives $L^*(H\alpha) = 2.1 \times 10^{42}$ ergs s $^{-1}$. The uncertainties on α and $L^*(H\alpha+[NII])$ are strongly correlated and depend upon the magnitude range of the fit; thus we do not present our parameters as an optimal choice, but merely as a way to compare the shape with previous work.

We can compare this luminosity function with other clusters, at lower redshift. The cluster A 521, at $z = 0.25$, was studied with a very similar technique, by Umeda et al. (2004). We adjust their published luminosity function to account for our different cosmology, and to remove their corrections for [NII] and dust extinction. We also apply a small rescaling to account for the difference in physical area considered, as Umeda et al. (2004) use a 2 Mpc radius, under a different cosmological model. The result is shown in the left panel of Fig. 12; the characteristic luminosity in their Schechter function fit with the above adjustments is $L^*(H\alpha+[NII]) = 3.9 \times 10^{41}$ ergs s $^{-1}$, a factor three fainter than in Cl 0024. We also compare with the luminosity functions of two other clusters, AC 114 ($z = 0.31$, Couch et al. 2001) and A 1689 ($z = 0.18$, Balogh et al. 2002b). These are based on deep spectroscopic observations made with the LDSS++ spectrograph on the Anglo-Australian Telescope, over a smaller field of view (7 arcmin, corresponding to a diameter of 1.3 Mpc in A 1689, and 1.9 Mpc in AC 114). To make a fair comparison, we show the luminosity functions within a radius of 0.80 Mpc, in the right panel of Fig. 12. The published AC 114 and A 1689 luminosity functions are multiplied by a small factor to approximately correct to a circular area of 0.80 Mpc radius. We also apply a correction for aperture bias by comparing the total I -band magnitudes to the magnitude within the spectroscopic aperture size. This amounts to a correction factor of ~ 1.4 . These luminosity functions are steeper than that of A 521, although with a similar characteristic luminosity. All three of these lower redshift clusters show $\gtrsim 4$ times fewer H α emitters of fixed luminosity than Cl 0024, within the same physical area. However, it is not clear whether this is due to a difference in cluster richness, or to a real evolutionary effect. In § 5 we will show the evolution of cluster SFR normalised to total cluster mass, to remove this degeneracy.

Finally, we compare our data with the field luminosity function at $z = 0.24$ and at $z \sim 0.7$. The lower redshift data are also obtained from a narrow-band Suprime-Cam survey (Fujita et al. 2003), and are in good agreement with the spectroscopically determined luminosity function at similar redshift (Tresse & Maddox 1998). The higher redshift luminosity function is obtained from spectroscopic measurements at the VLT (Tresse et al. 2002). After making the usual adjustments to remove the corrections for reddening and [NII] contribution, we renormalise to the expected average cluster density within R_{200} (left panel) and $0.47R_{200}$ (right panel). In the first case, the average cluster density is $200\rho_{\text{crit}}$, or ~ 670 times the average field density (for $\Omega_m = 0.3$), by definition. For the smaller radius, we use

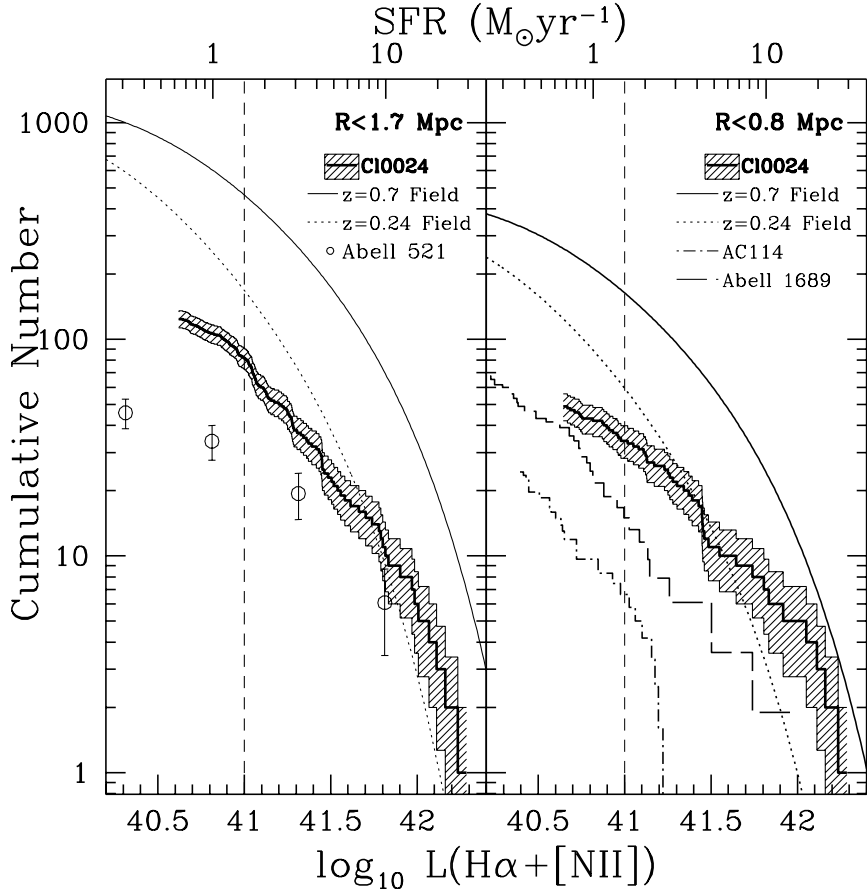


Figure 12. The $\text{H}\alpha$ luminosity function in Cl0024 and 1σ uncertainty (shaded region) within R_{200} (1.7 Mpc, left panel) and $0.47R_{200}$ (0.8 Mpc, right panel) of the cluster centre, uncorrected for dust extinction and $[\text{NII}]$ contamination. The vertical, dashed lines show the approximate completeness limit of our survey; fainter than this limit we underestimate the luminosity function. These results are compared with the Schechter function fits to the field luminosity functions at $z = 0.24$ (Fujita et al. 2003) and $z \sim 0.7$ (Tresse et al. 2002), renormalised to the theoretical overdensity of Cl0024 within the appropriate radius as described in the text. We also compare with the clusters A 521 ($z=0.25$, Umeda et al. 2004), AC114 ($z=0.31$, Couch et al. 2001) and A 1689 ($z=0.18$, Balogh et al. 2002b), as indicated in the legends.

the mass model of Kneib et al. (2003) to determine that the cluster overdensity is ~ 2260 times larger than the average field density. The $z = 0.24$ field $\text{H}\alpha$ luminosity function has a similar shape to the A1689 and AC114 clusters, with $L^*(\text{H}\alpha + [\text{NII}]) = 4.8 \times 10^{41}$ ergs s^{-1} . On the other hand, the $z \sim 0.7$ function is brighter, with $L^*(\text{H}\alpha + [\text{NII}]) = 6.3 \times 10^{41}$ ergs s^{-1} , and provides a close match to the Cl0024 data. In all cases, the renormalised field has $\gtrsim 5$ times more emitters of a given luminosity than clusters at similar redshifts. Therefore, we find that the shape of the $\text{H}\alpha$ luminosity function does not depend strongly on environment, although the normalisation does. There is significant evolution between $z \sim 0.2$ and ~ 0.4 , corresponding to a factor ~ 3 in $\text{H}\alpha$ luminosity. This degree of evolution is seen in both the field and cluster luminosity functions.

4.4 Trends with local density and cluster-centric radius

We will now consider how the $\text{H}\alpha$ distribution depends on the environment around Cl0024. In Fig. 13 we show the fraction of galaxies with $W_o(\text{H}\alpha + [\text{NII}]) > 40 \text{ \AA}$ as a func-

tion of local projected density and cluster-centric radius. We only consider galaxies brighter than $z' = 21.8$ because, fainter than this limit, the photometric errors scatter a significant number of galaxies with low equivalent widths to $W_o(\text{H}\alpha + [\text{NII}]) > 40 \text{ \AA}$ (see Fig. 2). Both the density and the strong emission line fraction are corrected for residual field contamination using the SDF control field. As expected, there is a decrease in the fraction of strong emission line galaxies with increasing density, toward the cluster centre. The same trend is seen for both bright and faint galaxies. At low densities, $\Sigma \lesssim 20 \text{ Mpc}^{-2}$, the statistical background correction dominates, and the uncertainties become large¹.

Thus, the fraction of strong emission line galaxies depends strongly on local environment. However, for those galaxies that are detected in emission, the equivalent width distribution and $\text{H}\alpha$ luminosity function are approximately independent of environment. This is shown in Fig. 14, where

¹ Note that the statistical nature of the background subtraction means the fraction of galaxies with $\text{H}\alpha$ emission can exceed unity at the lowest density end.

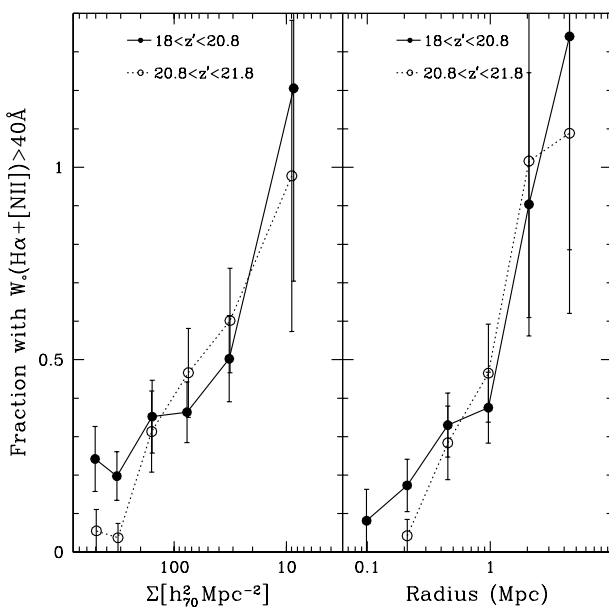


Figure 13. The fraction of galaxies with $W_o(H\alpha+[NII]) > 40 \text{ \AA}$, corrected for residual field contamination, is shown as a function of local projected density (left panel), and cluster-centric radius (right panel), for bright and faint galaxies separately.

we compare the H α luminosity functions for galaxies detected in H α within the highest density environments (excluding the NW group), with those at the lowest densities. We also show the data for galaxies in the NW group, which has an unusually high fraction of emission line galaxies, consistent with 100 per cent for blue galaxies (see below). The H α luminosity function shows little sensitivity to local density; although the cluster and group appear brighter by ~ 0.2 mag than the lowest density regions, this is only a $\sim 1\sigma$ difference. We conclude that emission line strength itself does not depend strongly on environment, and it is only the fraction of emitters that changes with density. The same conclusion was reached from observations of the local Universe, by Balogh et al. (2004b).

In Fig. 15 we compare the fraction of spiral and irregular galaxies (spectroscopic cluster members identified from *HST* images) with the field-corrected fraction of galaxies with significant H α emission, as a function of cluster-centric radius. Both samples are limited to $z' < 21.8$. As shown by Treu et al. (2003), the fraction of spiral and irregular galaxies increases sharply within the inner ~ 0.5 Mpc, and remains fairly constant at ~ 50 –60 per cent beyond that radius. In contrast with this, the fraction of galaxies detected in H α rises gradually with increasing radius, out to ~ 1 –2 Mpc, where it quickly increases to $\gtrsim 80$ per cent. This demonstrates that the trends in morphology and star formation are at least partly independent, and that the underlying mechanisms driving these trends may be different, as we discuss further in § 5.2.

The integrated broad-band colours of the galaxies trace star-formation on longer time-scales ($\gtrsim 0.5$ Gyr, although this is model and waveband dependent) than H α , and thus provide a useful comparison. Figure 16 shows the colour-magnitude diagrams for galaxies in two different environ-

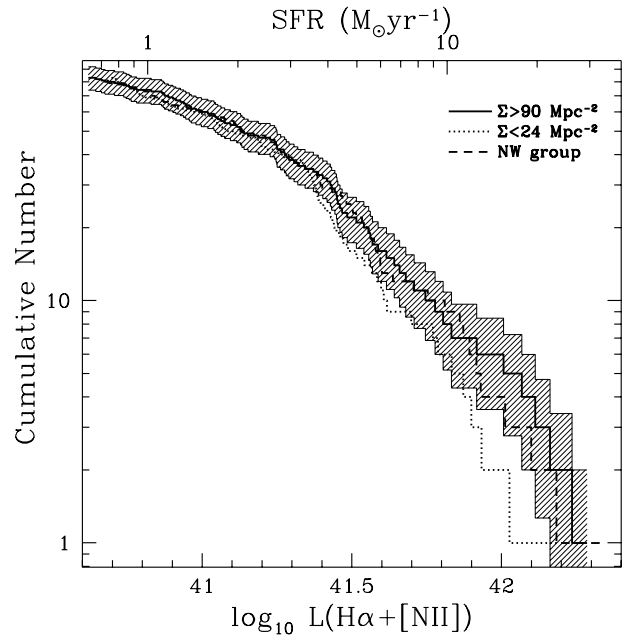


Figure 14. The H α luminosity function in the highest-density regions ($\Sigma > 90 \text{ Mpc}^{-2}$, but excluding the NW group), lowest-density regions ($\Sigma < 24 \text{ Mpc}^{-2}$), and in the NW group of galaxies. Each sample has 83 galaxies. The shaded region represents the $1-\sigma$ uncertainty on the luminosity function for the dense region, only.

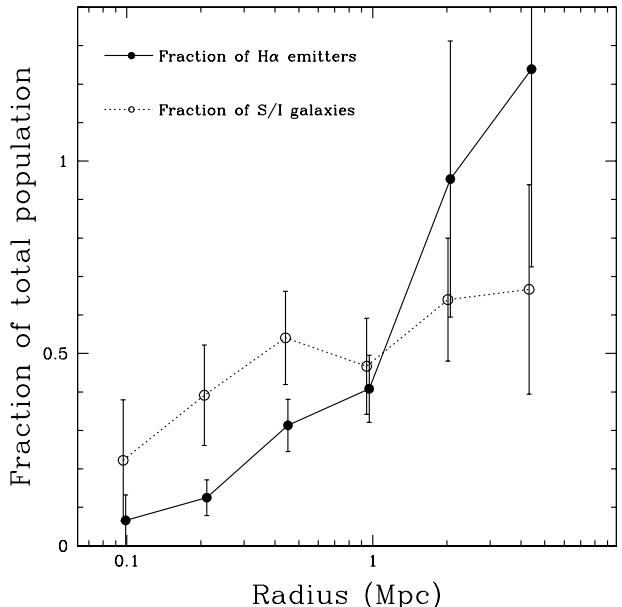


Figure 15. The solid circles show the fraction of galaxies detected in H α , statistically corrected for field contamination, as a function of cluster-centric radius. The open symbols show the fraction of spectroscopically-confirmed cluster members classified as spiral or irregular types by Treu et al. (2003); these points are offset in radius by a small amount for clarity. Both samples are restricted to magnitudes $z' < 21.8$.

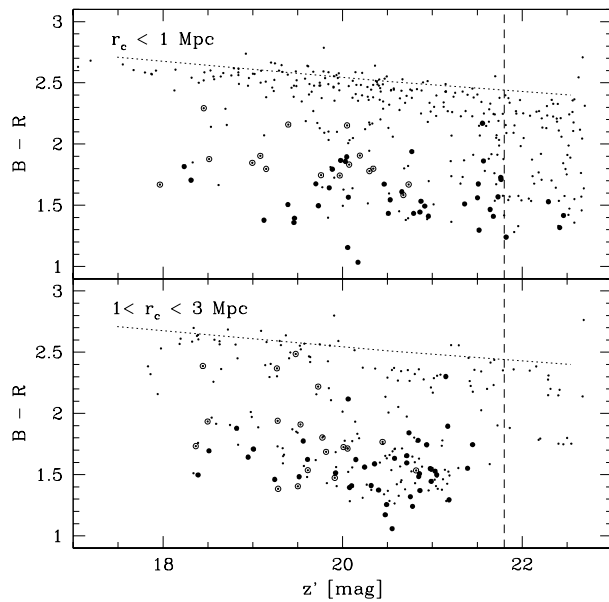


Figure 16. The field-corrected colour-magnitude diagrams of galaxies in the cluster core (top panel, $r_c < 1 \text{ Mpc}$) and in the outskirts (bottom panel, $1 < r_c < 3 \text{ Mpc}$). The residual contamination is removed. Galaxies detected with $W_o(\text{H}\alpha + [\text{NII}]) \geq 40 \text{ \AA}$ are shown as filled circles; weaker emission lines, with $W_o(\text{H}\alpha + [\text{NII}]) < 40 \text{ \AA}$, are shown as circled points and undetected galaxies are just points. The dotted line illustrates the colour-magnitude slopes of the Coma elliptical models (Kodama & Arimoto 1997). The vertical dashed line indicates $z' = 21.8$ below which the strong emitters become incomplete.

ments. As observed in the local Universe (e.g. Baldry et al. 2004; Balogh et al. 2004a) and at higher redshift (e.g. Bell et al. 2004) the galaxies form two distinct populations: a blue population with $B - R \sim 1.6$ (mostly showing emission) and a red population with $B - R \sim 2.4$ (having no or little emission), and a gap is seen in between. The relative proportion of these two populations depends strongly on environment. In the cluster core, the red colour-magnitude sequence is much more populated and well established than that seen in the outskirts, and the fraction of blue star forming galaxies is much lower. To see this environmental dependence more clearly and quantitatively, we plot the $(B - R)$ colour as functions of local density and cluster-centric distance in Fig. 17. To concentrate on the environmental dependence of colours, we correct for the slope of colour-magnitude relation (the dotted line on Fig. 16) on the red sequence using the models of Kodama & Arimoto (1997), denoted $(B - R)_c$, where

$$(B - R)_c = (B - R) + 0.043(z' - 20.2), \quad (2)$$

corresponding to the colour at $M^* + 1$ ($z' = 20.2$). The residual field contamination is corrected on these diagrams using the SDF control field data in the same manner as adopted in Kodama et al. (2001). The densities on the horizontal axis are also corrected for the contamination.

Again, the blue population dominates at low densities/outer regions, while the red population dominates at high densities/inner regions; in fact, within $\sim 200 \text{ kpc}$ of the centre, there are almost no blue galaxies. It is clearly

seen that the colour distribution of galaxies starts to become predominantly blue at low densities or at large radii from the cluster centre, as also seen in A 851 at $z = 0.41$ (Kodama et al. 2001). In fact, a transition from a predominantly blue population to one dominated by red galaxies is identified at around the virial radius (1.7 Mpc). Although a strong sequence of red galaxies is present in all environments, the blue galaxies quickly disappear within this radius, where the relative number of red galaxies is much larger than in the field populations (SDF), shown by the horizontal lines at the edge of the diagrams. This traces the trend observed in $\text{H}\alpha$ emission, shown in Fig. 15.

The galaxies with detected $\text{H}\alpha$ are preferentially blue; this is particularly true for the fainter population, where almost all the strong emission line galaxies are bluer than $(B - R)_c = 2$. On the other hand, the brighter galaxies show a significant population of red galaxies with detected emission. Almost all of these have only relatively weak emission, with $W_o(\text{H}\alpha) < 40 \text{ \AA}$, which would not be detectable in the fainter galaxies.

These correlations are shown also in Fig. 18, where we plot the colour distributions as a function of luminosity and environment. The bimodality in the colours is clear again here, as there are few galaxies with intermediate colours, $(B - R)_c \sim 2$ at any magnitude or in any environment. In a fixed magnitude range, the relative height of the two distributions is a strong function of density. Fig. 18 also shows the colour distribution of galaxies detected in $\text{H}\alpha$ emission; as expected, they are almost all blue galaxies. We have computed the fraction of blue galaxies [$(B - R)_c < 2$] with $W_o(\text{H}\alpha) > 40 \text{ \AA}$, corrected for residual field contamination, in each of our luminosity and environment bins. Approximately 30 ± 10 per cent of blue galaxies show strong $\text{H}\alpha$ emission with no strong dependence on luminosity or environment. The group of galaxies to the NW is therefore notable, in that it has a very high fraction of blue galaxies. In Fig. 19 we show the colour distribution of galaxies within 3.5 arcmin (1.1 Mpc) of this clump, corrected for residual background contamination. The population is statistically consistent with almost all the blue galaxies having strong $\text{H}\alpha$ emission, $W_o(\text{H}\alpha) > 40 \text{ \AA}$. We compare this with the galaxy population outside of this clump, but with similar local projected densities, $\Sigma = 22.8\text{--}40 \text{ Mpc}^{-2}$. Here, only 23 ± 4 per cent of the blue galaxies show $W_o(\text{H}\alpha) > 40 \text{ \AA}$. We note however that this difference can be due to the case that the NW clump has just right systemic velocity in the line of site so that the $\text{H}\alpha$ emission is neatly covered by the NB912 filter, whereas the regions outside of this NW clump may contain systems with different velocities so that $\text{H}\alpha$ detection is incomplete (Fig. 1).

5 DISCUSSION

5.1 Evolution

The dependence of $\text{H}\alpha$ emission on environment in the local Universe has recently been quantified over a large range of scales, using the 2dF galaxy redshift survey and the Sloan Digital Sky Survey (SDSS) (Lewis et al. 2002; Gomez et al. 2003; Balogh et al. 2004b). In particular, Balogh et al. (2004b) have shown correlations of galaxy population with local projected density, Σ_5 , which is computed

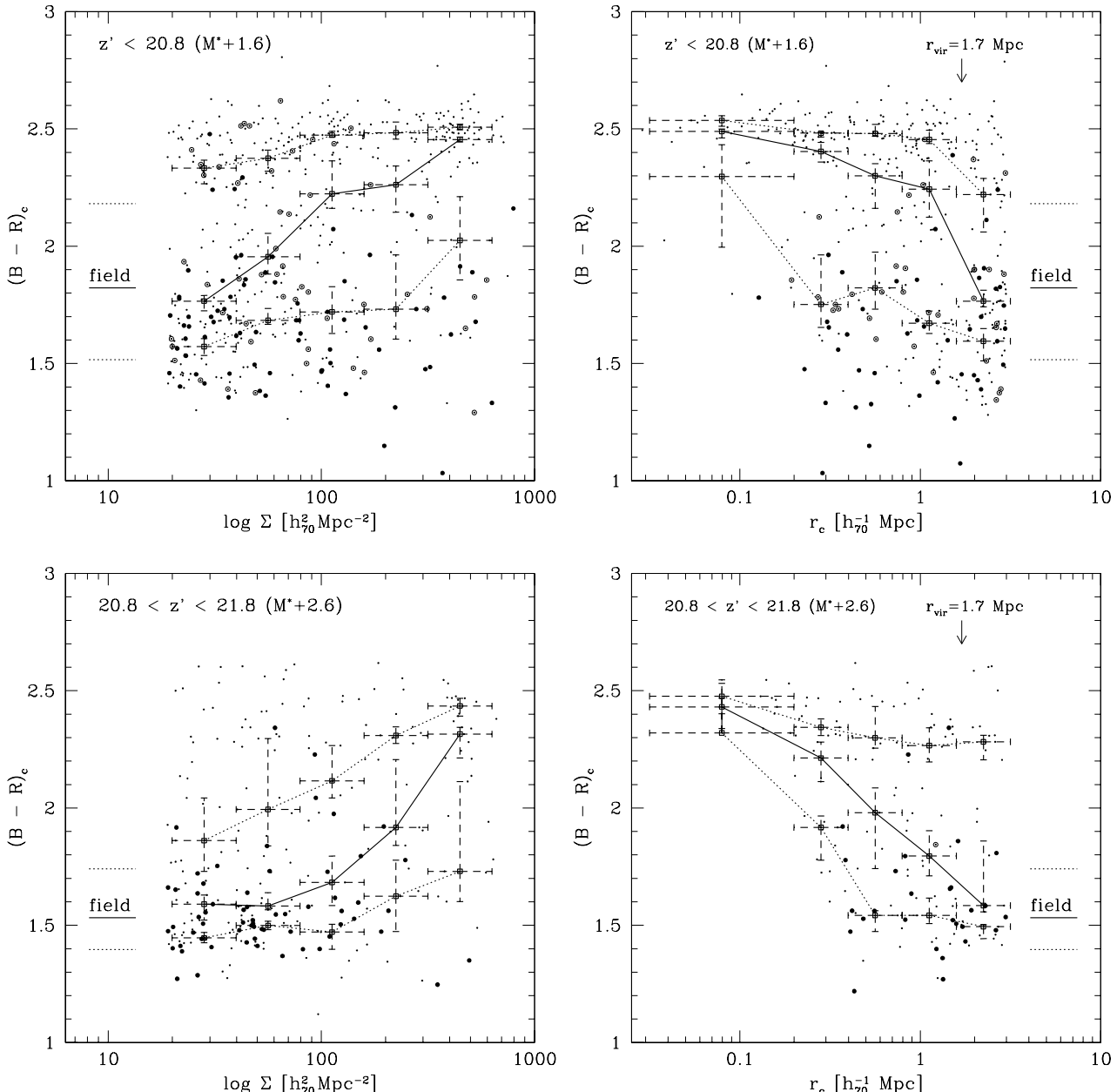


Figure 17. The background corrected colour distributions $(B - R)_c$ of galaxies as a function of local projected density (left panels) and cluster-centric radius (right panels) are shown for bright galaxies ($M < M^* + 1.6$, top panels) and faint galaxies ($M^* + 1.6 < M < M^* + 2.6$, bottom panels). The local density Σ is calculated for 10 nearest neighbours brighter than $z' = 22.7(M^* + 3.5)$ and the residual contamination is removed. Galaxies detected with $W_o(\text{H}\alpha + \text{[NII]}) \geq 40 \text{ \AA}$ are shown as filled circles; weaker emission lines, with $W_o(\text{H}\alpha + \text{[NII]}) < 40 \text{ \AA}$, are shown as circled points and undetected galaxies are just points. The three folded lines denote the 25th (upper dotted line), 50th (solid line) and 75th (lower dotted line) percentile colour loci with poissonian error-bars. The three horizontal lines at the edges show the percentile colours of galaxies in the SDF control field with $0.31 < z_{\text{phot}} < 0.45$, the same cut as used for the cluster.

from the distance to the fifth-nearest (projected) neighbour within 1000 km s^{-1} . They showed that the fraction of emission line galaxies decreases from ~ 60 per cent in low-density environments ($\Sigma_5 = 0.1 \text{ Mpc}^{-2}$) to ~ 10 per cent in the highest-density regions ($\Sigma_5 = 10 \text{ Mpc}^{-2}$). As discussed in § 3.4, our densities can be up to a factor of ~ 50 larger than theirs, because of the larger projected volume and the deeper photometry. With this correction (i.e. a factor of 50), our observed correlation between the fraction of galaxies with H α

emission and Σ (Fig. 13) is in good qualitative agreement with the local relation. A more precise comparison is difficult because, in addition to the uncertain correction to the density scale, Balogh et al. (2004b) measure the fraction of galaxies with $W_o(\text{H}\alpha) > 4 \text{ \AA}$, while our photometric uncertainties limit our analysis to the fraction with much stronger emission, $W_o(\text{H}\alpha + \text{[NII]}) > 40 \text{ \AA}$ (e.g. Fig. 13). Additional uncertainties are associated with the selection band and the magnitude range of the surveys. However, it appears that

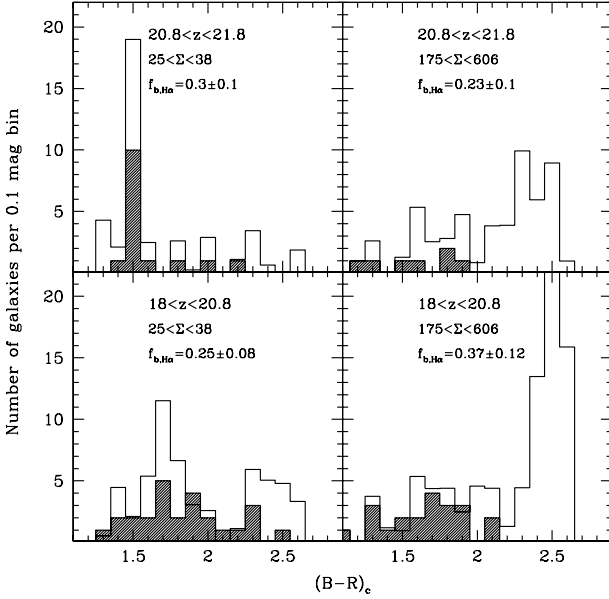


Figure 18. The $(B - R)_c$ colour distribution of Cl0024, as a function of luminosity and local, projected density (Σ , in units of Mpc^{-2}), is shown as the *open histograms*. The *solid histograms* show the subset of galaxies detected in $\text{H}\alpha$. In each panel, we label the value of $f_{b,\text{H}\alpha}$, which is the fraction of galaxies bluer than $(B - R)_c = 2$ with $W_o(\text{H}\alpha) > 40 \text{ \AA}$.

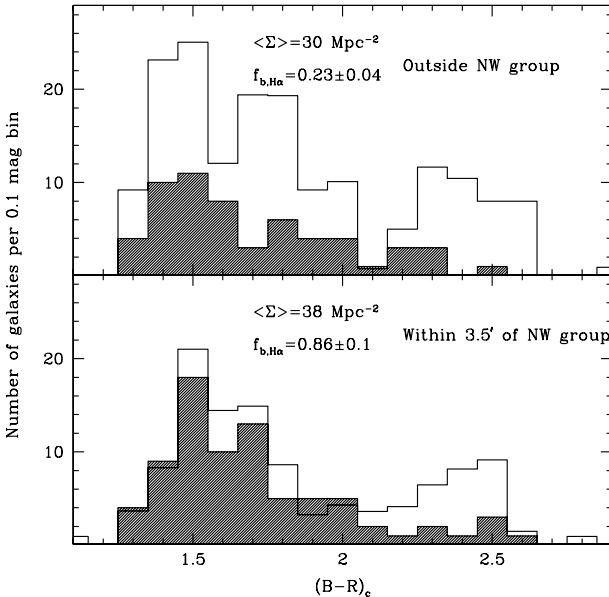


Figure 19. The background-corrected colour distribution of galaxies in the NW clump (*bottom panel*) and in regions outside this clump, but at similar local projected densities (*top panel*). The *shaded histograms* show the colour distribution of galaxies detected in $\text{H}\alpha$ emission. In each panel we label the average value of Σ , and the fraction of blue galaxies ($(B - R_c) < 2$) with $\text{H}\alpha$ emission.

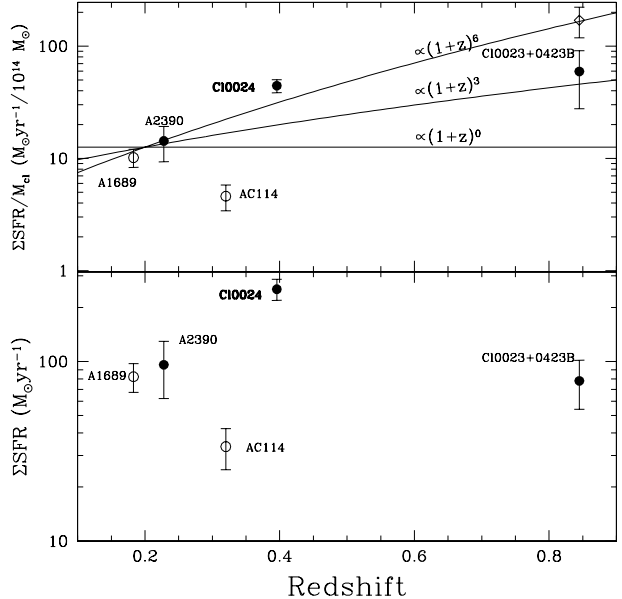


Figure 20. Bottom panel: The total SFR within $0.5 R_{200}$, is shown as a function of redshift for Cl0024 and four other clusters with deep $\text{H}\alpha$ observations, either from imaging data (solid circles) or aperture spectroscopy (open circles). **Top panel:** We show the total SFR within $0.5 R_{200}$ divided by the total mass M_{200} , for the same clusters. The uncertainties are based on the number of galaxies contributing to the sum, and do not include the uncertainties on the mass estimates. The diamond symbol shows the effect of assuming the mass estimate of Finn et al. (2004) for ClJ0023+0423B, rather than that of Postman et al. (1998). The solid lines shows different scalings with $(1 + z)$, as a guide.

the correlation between galaxy population and local density has not evolved radically between $z \sim 0.4$ and $z \sim 0.1$.

Recently, Finn et al. (2004) attempted to compare the total SFR within clusters as a function of redshift and velocity dispersion. To make a similar comparison, we measure the total amount of star formation within $0.5 R_{200}$, which corresponds to $\sim 0.85 \text{ Mpc}$ for Cl0024. Within this radius, we detect 56 galaxies and a total SFR of $\sim 253 \pm 34 \text{ M}_\odot \text{ yr}^{-1}$. Most of this SFR (> 97 per cent) comes from galaxies with $\text{SFR} > 1 \text{ M}_\odot \text{ yr}^{-1}$, where our sample is complete. Furthermore, even including all galaxies with $W_o(\text{H}\alpha + \text{[NII]}) > 0 \text{ \AA}$ in the total, a clear overestimate due to large photometric errors at faint magnitudes, only increases the total SFR by ~ 17 per cent. Therefore, we do not expect our incompleteness to have a large effect on this calculation.

Following Finn et al. (2004) we compare this number with the total SFR within $0.5 R_{200}$ of the clusters A 2390 (Balogh & Morris 2000), A 1689 (Balogh et al. 2002b), AC 114 (Couch et al. 2001), and ClJ0023+0423B (Finn et al. 2004). In so doing, we include a correction for sampling fraction and aperture bias for the spectroscopic results of A 1689 and AC 114, that was neglected by Finn et al. (2004); this amounts to an increase in the total SFR by a factor ~ 2.8 in these clusters. We adopt the R_{200} given by Finn et al. (2004), except for A 1689, where we take $R_{200} = 1.6 \text{ Mpc}$ from King, Clowe, & Schneider (2002).

In the bottom panel of Fig. 20, we first compare the total SFR within $0.5R_{200}$ of these five clusters. There is no apparent trend with redshift. There is a large scatter – with AC114 and Cl0024 differing by nearly an order of magnitude between the two clusters. We now follow Finn et al. (2004) and normalise these SFR totals by the cluster masses. For Cl0024, A1689 and AC114 we will use the lensing masses of $5.7 \times 10^{14} M_{\odot}$ (Kneib et al. 2003), $8.1 \times 10^{14} M_{\odot}$ (King, Clowe, & Schneider 2002), and $7.3 \times 10^{14} M_{\odot}$ (Natarajan et al. 1998), respectively. For A2390 we use the X-ray mass derived from *Chandra* observations, $13.6 \times 10^{14} M_{\odot}$ (Allen, Ettori, & Fabian 2001), and for Cl J0023+0423B we take the average of the projected and annular mass estimates within 714 kpc (Postman et al. 1998), and apply a small correction to scale the mass to $R_{200} = 614$ kpc. This gives a mass of $2.3 \pm 1.2 \times 10^{14} M_{\odot}$, where the uncertainty includes an estimate of the systematic uncertainty, taken to be the difference between the projected and annular mass measurements. The results are shown in the top panel of Fig. 20, and again show a strong scatter – which likely exceeds any redshift evolution within the sample. We limit the evolution to be a factor ~ 4 out to $z \sim 0.8$. However, we have not accounted for systematic uncertainties in the mass estimates, which can be important because they are not all calculated using the same technique. In fact, Finn et al. (2004) claimed to find a stronger trend in normalised SFR with redshift; this is due to the use of mass estimates based on a simple scaling of velocity dispersion or X-ray luminosity. In particular, their dynamical mass estimate (based on a simple scaling of velocity dispersion) for Cl J0023+0423B is a factor $\sim 2\text{--}4$ lower than the one we have derived from Postman et al. (1998); adopting this mass gives the diamond point in Fig. 20 and implies stronger evolution out to $z \sim 0.8$.

On the basis of these five clusters it is not possible to draw strong conclusions about the amount of evolution in the mass-normalised SFR in clusters. The data suggest a large range in the total SFR per unit cluster mass at a fixed redshift, with limits on the evolution with redshift which are comparable to or even stronger than that seen in the general field (e.g. Lilly et al. 1996; Wilson et al. 2002). However, any evolutionary trend is particularly sensitive to the mass estimate for Cl0023J+0423B, and would have to ignore the low SFR in AC114. Although the results are intriguing, a larger sample of clusters is clearly needed. Furthermore, the sensitivity of H α to instantaneous star formation may mean that tests such as the above are strongly affected by small changes in the recent dynamic history of the cluster, for example. Averaging over larger cluster samples (or using indicators of star formation over longer time-scales) will allow us to overcome this sensitivity.

5.2 Galaxy transformations?

A possible explanation for the observed trends with local density and radius is that interactions with the surrounding environment transform galaxies from one type to another. Below we discuss specific observations which support this hypothesis and help to constrain the underlying mechanisms.

5.2.1 The shape of the H α luminosity function

We found that the distribution of H α strengths, for those galaxies detected in H α , is not strongly dependent on environment. A similar phenomenon is observed at low redshift, both in terms of galaxy SFR (Balogh et al. 2004b) and colours (Balogh et al. 2004a). Since the fraction of emission line galaxies depends strongly on local environment, this means that any transformation in galaxy properties must occur on a short time-scale, so that a substantial population of galaxies with low but present star formation is never dominant. For example, if transformations occur at a uniform rate with redshift, and are due to a decline in star formation over a time-scale of $\gtrsim 1$ Gyr, the fraction of galaxies in a transition state at any given epoch would be $1/13.7 = 7.3$ per cent, assuming a Hubble time of 13.7 Gyr. Although this is a small fraction of the total population, in dense environments (where few galaxies are forming stars at any rate) it would represent a large proportion of those galaxies detected in H α . At $\Sigma > 90 \text{ Mpc}^{-2}$, only ~ 35 per cent of galaxies are detected in H α and, in the above model, we would expect ~ 21 per cent of them to have abnormally low SFR; this would easily be detectable as a change in the shape of the H α luminosity function. Therefore, we suggest that the time-scale for truncating star formation must be < 1 Gyr. An alternative explanation is that the transformations occurred at much earlier times; however, the strong evolution in the fraction of star forming galaxies relative to $z = 0$ clusters makes this seem unlikely.

5.2.2 Passive spiral galaxies

The presence of spiral galaxies with little or no star formation, which we call “passive spirals”, are the most direct evidence we have that galaxies may transform from one morphological type to another via changes to the SFR (e.g. Couch et al. 1998; Poggianti et al. 1999; Balogh et al. 2002a). Recently, Goto et al. (2003b) have suggested, using SDSS data, that such galaxies are associated with the infall regions of clusters. Of the 63 spectroscopic member galaxies in Cl0024 with spiral morphologies (classification 3–6) as determined from *HST* data, 22 (35 ± 7 per cent) are undetected in H α emission. This is a much larger fraction than the 0.28 per cent found in the local field Goto et al. (2003b), and consistent with the ~ 20 per cent observed in distant clusters (Poggianti et al. 1999). Most of the passive galaxies in our sample are actually detected in H α absorption over the full spatial extent, and two are post-starburst galaxies (see below). None of the galaxies are detected spectroscopically in [OII] (Czoske et al. 2001), and they are found throughout the cluster region, with no preference for either the centre or the outskirts. These galaxies have a range of colours, though most are quite red, and only 8/22 (36 per cent) are bluer than $(B - R)_c = 2.0$.

This supports a scenario in which environmentally-induced changes to the SFR are at least partially independent from morphological changes and, in particular, that star formation is the more sensitive of the two. It is possible that some morphological transformation occurs on a longer time-scale, by the fading of a disk in which star formation has stopped (Bekki, Couch, & Shioya 2002). An alternative possibility is that the truncation of star formation and mor-

phology is driven by different physical mechanisms. This is supported by our results that show the truncation of star formation may take place at large radii, $\gtrsim 1$ Mpc, while the fraction of spiral and irregular galaxies remains constant beyond ~ 0.5 Mpc. This may suggest that the SFR responds quickly when galaxies reach the outskirts of clusters, while another physical mechanism(s), such as harassment (Moore et al. 1999), may play a role in transforming the morphologies later on when the galaxies approach further inside the cluster core. If the decline of SFR was more gradual, the trend with density would be less sharp, and the distinction from the morphological trend would be less clear.

5.2.3 Galaxies with strong $H\delta$ absorption

Finally, we consider another unusual class of galaxy, comprised of those with atypically strong $H\delta$ absorption. In particular, the existence of such galaxies without the expected emission lines arising from ionized gas have been invoked as evidence for a recent truncation of star formation, perhaps preceded by a starburst (Dressler & Gunn 1982; Couch & Sharples 1987; Poggianti et al. 1999; Goto et al. 2003a). In Fig. 21 we show the correlation between $W_o(H\alpha+[NII])$ and $W_o(H\delta)$, for spectroscopically confirmed cluster members. The $H\delta$ measurements are taken from the spectroscopic catalogue of Czoske et al. (2001); this line is measured only for those galaxies in which it is particularly strong. Of the 243 spectroscopic members, 9 (4 ± 1 per cent) have $W_o(H\delta) > 4$ Å and no detectable emission, approximately consistent or slightly larger than the fraction in clusters at similar redshifts (e.g. Poggianti et al. 1999; Tran et al. 2003). All of these galaxies are located > 3 arcmin (> 1 Mpc) from the cluster centre. Unfortunately, the interpretation of these galaxies is not straightforward, as a simple cut in $W_o(H\delta)$ is insufficient to constrain the star formation history without ambiguity. However, it is clear that the data are at least consistent with a substantial population of post-starburst galaxies. Since the duty cycle of such galaxies is likely to be short, even a small population can be indicative of a more widespread phenomenon. The existence of these galaxies, and the passive spiral galaxies noted above, are good evidence that short time-scale transformations are taking place in the field around Cl 0024. However, there are too few to pinpoint any particular environment as the cause.

In addition, we see a very small number of galaxies with $W_o(H\delta) > 4$ Å and $W_o([OII]) < 10$ Å, but which exhibit strong $H\alpha$ emission, $W_o(H\alpha+[NII]) \geq 30$ Å (these are some of the galaxies lying below the correlation in Fig. 4). These apparently post-starburst galaxies are likely to be highly-obscured, starbursts (where the $[OII]$ emission is suppressed by dust) similar to those discussed by Smail et al. (1999) and Poggianti & Wu (2000).

5.2.4 Summary

All the above evidence implies that any transformations occurring in the galaxy star formation rate must take place on relatively short time-scales, in a manner that is independent of the morphological transformation. The fact that the fraction of star-forming galaxies is reduced so far from the

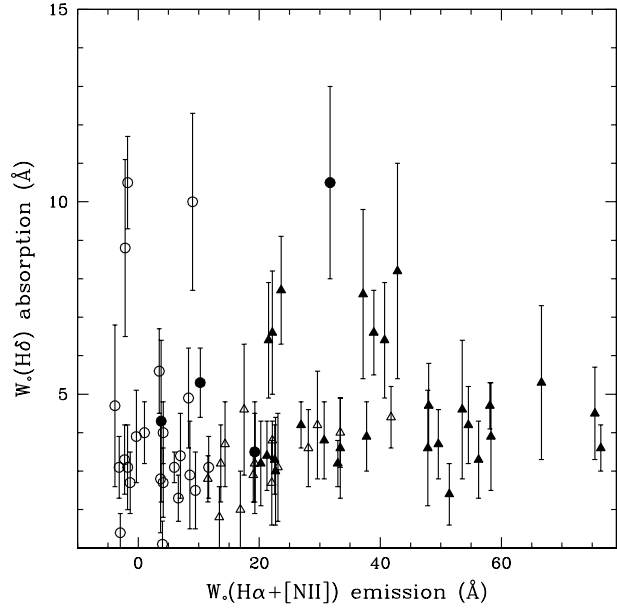


Figure 21. The $H\delta$ absorption line equivalent width, from the spectroscopic sample of Czoske et al. (2001), is shown as a function of $W_o(H\alpha+[NII])$, for spectroscopically-confirmed cluster members. *Triangles* are $H\alpha$ detections, while *circles* are non-detections. *Open symbols* have $[OII]$ equivalent widths < 10 Å, while *filled symbols* have detectable emission with > 10 Å. $1-\sigma$ error bars are shown on $H\delta$ only, for clarity.

cluster centre ($\gtrsim 1$ Mpc) means that ram pressure stripping of the cold gas through interaction with the intra-cluster medium (Gunn & Gott 1972) is unlikely, although a significant fraction of galaxies at this radius may have already passed through the cluster core (Mamon et al. 2004; Gill et al. 2004). A second possibility is that galaxy-galaxy interactions induce transformations (e.g. Moore et al. 1999; Hashimoto & Oemler 2000; Lambas et al. 2003), although the fact that the morphological transformation appears to be decoupled from the decline in star formation may prove a challenge for this interpretation. A final possibility are the so-called strangulation models (Larson, Tinsley, & Caldwell 1980; Balogh, Navarro, & Morris 2000) in which a purported halo of hot gas is stripped from galaxies in dense environments, leading to a gradual winding down of star formation as the remaining cold, disk gas is consumed. Although this may be effective in relatively low density environments, the time-scale for the truncation of star formation is typically $\gtrsim 1$ Gyr, which may be too long to accommodate our observations that the shape of the $H\alpha$ luminosity function is insensitive to environment.

The fact that the correlation between galaxy properties and local density is already in place in this cluster at $z = 0.4$, in a sense that is qualitatively similar to that observed at $z = 0$, may mean that the predominant transformation mechanism occurs before galaxies are accreted into clusters.

6 CONCLUSIONS

We have used deep, panoramic multicolour imaging of Cl 0024.0+1652 to trace the galaxy population from the cluster core to the outskirts. We find the following:

1. The correlation between galaxy star formation rate and local environment is already well established in Cl 0024 ($z \sim 0.4$). The fraction of galaxies detected in H α is a strong function of local projected density and cluster-centric radius. The sense and magnitude of this trend is qualitatively similar to that seen at low redshift (Balogh et al. 2004b).

2. The shape of the H α luminosity function is generally independent of environment, and consistent with the $z \sim 0.7$ field luminosity function of Tresse et al. (2002). However, we detect a factor ~ 3 brightening in the characteristic luminosity relative to lower redshift clusters and the $z \sim 0.24$ field (Balogh & Morris 2000; Couch et al. 2001; Balogh et al. 2002b; Umeda et al. 2004).

3. The cluster core has a significant population (35 ± 7 per cent) of spiral galaxies without H α emission, consistent with other clusters at similar redshifts (Poggianti et al. 1999). There is also a small population of post-starburst galaxies in the outskirts of the cluster.

4. The fraction of galaxies with significant star formation depends on environment far ($\gtrsim 1$ Mpc) from the cluster, while the fraction of spiral and irregular galaxies is only sensitive to environment within the inner ~ 0.5 Mpc. This suggests that the two correlations may not entirely arise from the same underlying physical mechanisms.

5. Through a comparison with other studies of H α emission in clusters out to $z = 0.8$, we find that the total SFR within $0.5R_{200}$ and the SFR normalised to total cluster mass both show a large cluster-to-cluster variation with no detectable dependence on redshift, although it would be possible for the latter to evolve as strongly as $(1+z)^6$ (given the large scatter). However, this is dependent on the uncertain mass measurement of the most distant cluster.

We conclude that the decrease in star formation activity in dense environments is likely due to the decline in SFR on relatively short time-scales, before mechanisms such as galaxy harassment transform the morphology of the galaxy. The actual mechanism responsible for truncating the star formation may occur even before galaxies are accreted into clusters.

ACKNOWLEDGEMENTS

We thank Oliver Czoske for providing his spectra for comparison and Tommaso Treu for providing the reduced HST images. We acknowledge the Suprime-Cam team for allowing us to use the narrow-band filter, NB₉₁₂, prior to open to the public. We thank Rose Finn for helpful discussions. We also acknowledge the SDF team for allowing us to use their data as a control field to correct for the field contamination in our analysis. This work is based on data collected at Subaru Telescope, which is operated by the National Astronomical Observatory of Japan, and was financially supported in part by a Grant-in-Aid for the Scientific Research (No. 15740126) by the Japanese Ministry of Education, Culture, Sports, Science and Technology. TK acknowledges the Physics Depart-

ment at University of Durham for their kind hospitality during the course of this work. Similarly, MLB thanks the NAOJ for their hospitality. MLB and RGB acknowledge financial support from PPARC Research and Senior Fellowships, respectively. IRS acknowledges support from the Royal Society.

REFERENCES

Afonso J., Hopkins A., Mobasher B., Almeida C. 2003, ApJ, 597, 269
 Allen S. W., Ettori S., Fabian A. C. 2001, MNRAS, 324, 877
 Baldry I. K., Glazebrook K., Brinkmann J., Ivezić Z., Lupton R. H., Nichol R. C., Szalay A. S. 2004, ApJ, 600, 681
 Balogh M., Bower R. G., Smail I., Ziegler B. L., Davies R. L., Gaztelu A., Fritz A. 2002a, MNRAS, 337, 256
 Balogh M. L., Baldry I. K., Nichol R. C., Miller C., Bower R. G., Glazebrook K. 2004a, ApJL, submitted
 Balogh M. L., Couch W. J., Smail I., Bower R. G., Glazebrook K. 2002b, MNRAS, 335, 10
 Balogh M. L., Morris S. L. 2000, MNRAS, 318, 703
 Balogh M. L., Morris S. L., Yee H. K. C., Carlberg R. G., Ellingson E. 1997, ApJL, 488, 75
 Balogh M. L., Navarro J. F., Morris S. L. 2000, ApJ, 540, 113
 Balogh M. L. et al. 2004b, MNRAS, 348, 1355
 Barger A. J. et al., 1998, ApJ, 501, 522
 Bekki K., Couch W. J., Shioya Y. 2002, ApJ, 577, 651
 Bell E. F. et al. 2004, ApJL, 600, L11
 Bertin E., Arnouts S. 1996, A&AS, 117, 393
 Blanton M. R. et al. 2003, ApJ, 592, 819
 Brinchmann J., Charlot S., White S. D. M., Tremonti C., Kauffmann G., Heckman T., Brinkmann J. 2003, MNRAS, in press, astro-ph/0311060
 Butcher H., Oemler A. 1978a, ApJ, 219, 18
 —. 1978b, ApJ, 226, 559
 Coia D. et al. 2004, A&A, submitted, astro-ph/0310317
 Couch W. J., Balogh M. L., Bower R. G., Smail I., Glazebrook K., Taylor M. 2001, ApJ, 549, 820
 Couch W. J., Barger A. J., Smail I., Ellis R. S., Sharples R. M. 1998, ApJ, 497, 188
 Couch W. J., Newell E. B. 1984, ApJS, 56, 143
 Couch W. J., Sharples R. M. 1987, MNRAS, 229, 423
 Czoske O., Kneib J.-P., Soucail G., Bridges T. J., Mellier Y., Cuillandre J.-C. 2001, A&A, 372, 391
 Dressler A., Gunn J. E. 1982, ApJ, 263, 533
 —. 1992, ApJS, 78, 1
 Dressler A. et al., 1997, ApJ, 490, 577
 Dressler A., Smail I., Poggianti B. M., Butcher H., Couch W. J., Ellis R. S., Oemler A. J. 1999, ApJS, 122, 51
 Finn R. A., Zaritsky D., McCarthy D. W. 2004, ApJ, 604, 141
 Fisher D., Fabricant D., Franx M., van Dokkum P. 1998, ApJ, 498, 195
 Fujita S. S. et al., 2003, ApJL, 586, L115
 Gill S. P. D., Knebe A., Gibson B. K. 2004, preprint, (astro-ph/0404427)
 Gomez P. L. et al. 2003, ApJ, 584, 210
 Goto T. et al. 2003a, PASJ, 55, 771

Goto T. et al. 2003b, PASJ, 55, 757

Gunn J. E., Gott J. R. 1972, ApJ, 176, 1

Hashimoto Y., Oemler A. J. 2000, ApJ, 530, 652

Hogg D. W. et al. 2004, ApJL, 601, L29

Hopkins A. M., Connolly A. J., Haarsma D. B., Cram L. E. 2001, AJ, 122, 288

Hopkins A. M. et al. 2003, ApJ, 599, 971

Jansen R. A., Fabricant D., Franx M., Caldwell N. 2000, ApJS, 126, 331

Kennicutt R. C. 1992, ApJ, 388, 310

Kennicutt R. C., Tamblyn P., Congdon C. E. 1994, ApJ, 435, 22

Kewley L. J., Geller M. J., Jansen R. A. 2004, AJ, 127, 2002

King L. J., Clowe D. I., Schneider P. 2002, A&A, 383, 118

Kneib J. et al., 2003, ApJ, 598, 804

Kodama T., Arimoto N. 1997, A&A, 320, 41

Kodama T., Arimoto N., Barger A. J., Aragon-Salamanca A. 1998, A&A, 334, 99

Kodama T., Bell E. F., Bower R. G. 1999, MNRAS, 302, 152

Kodama T., Smail I., Nakata F., Okamura S., Bower R. G. 2001, ApJL, 562, L9

Koo D. C., Guzmán R., Gallego J., Wirth G. D. 1997, ApJ, 478, 49

Lambas D. G., Tissera P. B., Alonso M. S., Coldwell G. 2003, MNRAS, 346, 1189

Landolt A. U. 1992, AJ, 104, 340

Larson R. B., Tinsley B. M., Caldwell C. N. 1980, ApJ, 237, 692

Lewis I. J. et al. 2002, MNRAS, 333, 279

Lilly S. J., Le Fevre O., Hammer F., Crampton D. 1996, ApJL, 460, L1

Maihara T. et al. 2001, PASJ, 53, 25

Mamon G. A., Sanchis T., Salvador-Solé E., Solanes J. M. 2004, A&A, 414, 445

Moore B., Lake G., Quinn T., Stadel J. 1999, MNRAS, 304, 465

Natarajan P., Kneib J., Smail I., Ellis R. S. 1998, ApJ, 499, 600

Poggianti B. M., Smail I., Dressler A., Couch W. J., Barger A. J., Butcher H., Ellis R. S., Oemler A. J. 1999, ApJ, 518, 576

Poggianti B. M., Wu H. 2000, ApJ, 529, 157

Postman M., Lubin L. M., Oke J. B. 1998, AJ, 116, 560

Schneider D. P., Dressler A., Gunn J. E. 1986, AJ, 92, 523

Smail I., Dressler A., Couch W. J., Ellis R. S., Oemler A., Butcher H., Sharples R. M. 1997, ApJS, 110, 213

Smail I., Morrison G., Gray M. E., Owen F. N., Ivison R. J., Kneib J.-P., Ellis R. S. 1999, ApJ, 525, 609

Trager S. C., Worthey G., Faber S. M., Burstein D., Gonzalez J. J. 1998, ApJS, 116, 1

Tran K. H., Franx M., Illingworth G., Kelson D. D., van Dokkum P. 2003, ApJ, 599, 865

Tresse L., Maddox S., Loveday J., Singleton C. 1999, MNRAS, 310, 262

Tresse L., Maddox S. J. 1998, ApJ, 495, 691

Tresse L., Maddox S. J., Le Fèvre O., Cuby J.-G. 2002, MNRAS, 337, 369

Treu, T. Ellis R. S., Kneib J., Dressler A., Smail I., Czoske O., Oemler A., Natarajan P. 2003, ApJ, 591, 53

Umeda K. et al. 2004, ApJ, 601, 805

van Dokkum P. G., Franx M. 1996, MNRAS, 281, 985

Wilson G., Cowie L. L., Barger A. J., Burke D. J. 2002, AJ, 124, 1258

Yagi M. 1998, PhD thesis, Univ. Tokyo

This figure "Fig8.jpg" is available in "jpg" format from:

<http://arxiv.org/ps/astro-ph/0408037v3>

This figure "Fig11.jpg" is available in "jpg" format from:

<http://arxiv.org/ps/astro-ph/0408037v3>